Vortex-induced piezoelectric cantilever beam vibration for ocean wave energy harvesting via airflow from the orifice of oscillation water column chamber

Xiaozhen Du[a]*, Yu Wang[a], Haixiang Chen[a], Chicheng Li[a], Yi Han[a], Daniil Yurchenko[c], Junlei Wang[d]*, Hong Yu[b]*

a College of Mechanical and Electronic Engineering, Shandong University of Science and Technology, Qingdao 266590, Shandong Province, P. R. China

b College of Science, China University of Petroleum, Qingdao 266580, Shandong Province, P. R. China

c Institute of Sound and Vibration Research, University of Southampton, Southampton SO17 1BJ, UK

d School of Mechanical and Power Engineering, Zhengzhou University, Zhengzhou, 450001, Henan Province, P. R. China

*Corresponding author: duxz@sdust.edu.cn (X. Du) jlwang@zzu.edu.cn (J.Wang) hongyu@upc.edu.cn(H.Yu),

Abstract: Micro piezoelectric generators have attracted immense interest to convert mechanical vibrations into electric energy for ultralow power wireless sensors. Herein, an ocean wave vortex-induced vibration piezoelectric energy harvester(Wave-VIVPEH) is proposed to extract wave energy. The renewable and sustainable ocean environment energy harvesting device consists of an oscillating water column(OWC) air chamber, wind tunnel, and piezoelectric energy converter. A fixed bluff body in the vent tunnel induces airflow vortexes and excites the piezoelectric cantilever vibration converting up the ultralow frequency of ocean waves. The novel Wave-VIVPEH is a complex multi-physics system requiring feasible methodologies to enhance its performance. The theoretical models are derived to systematically investigate and optimize the operation. The flume and wind tunnel experiments and the related fluid-solid electric coupling simulations are carried out to verify the concept's feasibility. The aerodynamic kinetic performance in the OWC chamber is characterized by the models. The instantaneous maximum exhalation airspeed reaches 16.55 m/s with the air pressure of 349.97 Pa and the wave period of T=2.5 s. In this wave condition, the results are well agreed with the simulation values of wind speed of 17.96 m/s, and air pressure of 382.55 Pa. The output power characteristics of the piezoelectric energy harvester are analyzed for the distance of the vortex wake between the piezoelectric cantilever beam and the bluff body. With the bluff body diameter of 25 mm and distance of d/d_D=4, the theoretical results on the maximum peak voltage and output power are 10.46 V, 3.26mW agree with the simulation optimized values of the maximum peak voltage of 10.85V and the output power of 3.55 mW. When the wind speed is 15 m/s, the theoretical voltage of 8.62 V approaches the experimental result of 8.47 V. Especially, the comparisons of the theoretical power and voltage to experimental and simulational results indicate that the ingenious Wave-VIVPEH has great potential in ocean wave energy harvesting applications to supply power for intelligent buoys.

Keywords: Piezoelectric energy harvesting(PEH); Ocean wave energy; Oscillating water column (OWC); Vortex-induced vibration(VIV); Bluff body; Intelligent buoy

1 Introduction

The wireless sensor nodes play an increasingly important role in real-time marine monitoring and protection. Compared with traditional battery and wired energy supply for the micropower consumption sensors, it is effective to explore the long-life and continuous electric power by employing wave energy harvesters[1]. At present, small-scale energy harvesters have been a globally appealing topic in items of research and practical application opportunities[2-4]. Ocean wave energy harvesting technology has been historically struggling to break through a commercial implementation[5, 6]. In particular, the oscillating water column(OWC) device is considered to be safe and reliable because the electric conversion element is protected against ocean water corrosion[6, 7]. It has been extensively exploited and implemented due to its mechanical and structural simplicity. OWC extracts the wave mechanical kinetic energy with the air chamber apparatus[5, 8], and the airflows circulate from the inner of the chamber to the outside[6]. Although the widespread electric generation utilizes electromagnetic air turbine power generation[9, 10], the complex turbomachines and electromagnetic converters are unsuitable micropower for wireless sensors in a small size structure. In recent years, various energy converting mechanisms have been proposed with the increasing popularity of micropower[11], for example, electrostatic[12-14], electromagnetic[15], dielectric[16, 17], triboelectric[18] and piezoelectric generation[19, 20]. Piezoelectric energy harvesting(PEH) utmostly has been the most prominent mechanical conversion mechanism compared to all of the others[21]. A flexible piezoelectric device (FPED) is developed to collect flow-induced vibration energy from the ocean and wind environment[22]. Based on the large deformation performance of polymer, although a novel dielectric elastomeric wave generator was designed with a U-oscillating water column (U-OWC) chamber to exploit drastic wave energy harvesting[23], the piezoelectric generators are more sensitive to strain with inherent electromechanical coupling coefficients that output higher electric power density. Moreover, various energy harvesting structures are exploited to integrate into the microelectromechanical system(MEMS) as self-power nodes. Especially in the ocean, the piezoelectric materials with characteristics of ceramic or polymer, such as PZT(Lead Zirconate Titanate) and PVDF (Polyvinylidene Fluoride), are not affected by humidity and corrosion[20, 24]. The piezoelectric cantilever beams are simple and conventional coupled structures for vibration and fluid energy harvesting[25]. They are clamped on the center pillar of the buoy to convert ocean wave energy into electricity[26]. When the natural frequency of the cantilever beam matches the excitation frequency, achieving resonance, the oscillation displacement and strain sharply increase. Therefore, the energy harvesting device generates a higher voltage and more charges on the surface of the piezoelectric beam[27]. A vertical piezoelectric cantilever vibrator is developed with a crank-slider mechanism to investigate combination parametric resonance under harmonic excitation[28]. An efficient cylinder energy harvester is composed of a series of L-shaped piezoelectric coupled beams that array around the circum[29]. Although the aforementioned piezoelectric generators are effective in vibration energy harvesting, the natural frequencies of the cantilever beams are too high for the ultralow frequencies of ocean waves which are usually spread in the range of 0.03-1Hz[30]. The ingenious mechanical equipment types convert up the ultra-low-frequency motion into a continuous rotation or rectilinear motion and then forward a high-frequency exciting motion for the electric power converters[31, 32]. A geared-linkage mechanism with the piezoelectric film[33] and a teeth rack coupling with the piezoelectric beams are proposed respectively to increase the wave motion frequency[34]. The excitation frequencies hardly resonate with the piezoelectric beams because the increment ratio is

a constant of the teeth number. In addition, the piezoelectric materials, such as a well-known PZT ceramic are brittle, i.e. can be easily broken by rigid mechanical interaction. The frequency range of wave mechanical vibrations usually varies with time. Therefore, it is essential to explore suitable mechanisms and couple the irregular wave and soft-contact piezoelectric conversion body. On a floating buoy, two piezoelectric levers were respectively connected to both ends of a mass-spring as a flexible system that adapts for the various wave periods[35]. Piezoelectric stack transducer in d_{33} mode is pre-loaded by dynamic magnetic force that increases output power more than a thousand times[36]. Although the above-mentioned output electric powers have been significantly improved, the vibration frequencies are far below the resonance of piezoelectric structures.

In general, the resonance is efficient for energy conversion because the piezoelectric harvester vibrates intensely in the vicinity of inherent frequency, especially for the cantilever beam[37]. Moreover, the output power increases with the oscillation frequency of piezoelectric cantilever beams[38]. Contrary to the statement above, the inherent frequencies of piezoelectric cantilever beams are usually tens to hundreds of hertz that are far above the ocean wave frequencies[39]. Consequently, it is insufficient to match the frequency of each other in resonance mode based on the mechanical structure adjustment. Considerable research efforts have been devoted to improving piezoelectric energy harvester (PEH) performance. The low-frequency kinetic exciting sources usually are converted into high-frequency motion. Oscillating systems of electric generation on the water by the mean of an air chamber for absorbing waves usually include several steps in the process of converting the low-frequency wave energy to some useful form. The extraction of ocean wave energy is the first step to converting the wave motion into kinetic airflow by OWCs[40].

Vortex-induced vibration (VIV) has been an efficient method for fluid kinetic energy harvesting[41]. It can significantly enhance the structural vibration performance to harvest low-frequency vibration energies[42]. A significant number of review papers have been conducted to investigate different techniques and mechanisms to enhance the level of the harvested power in high-frequency vibration, e.g. flutter[43, 44], galloping[45-47], and vortex-induced instability acting[48]. Furthermore, the vibration of the PEH response depends on the quantity and form of the bluff bodies and the fluid properties. A new type of wake-induced vibration is proposed to analyze the output power peculiarity on different bluff bodies, such as round, normal, and inverted D-shaped cylinders [49]. In addition, COMSOL Multiphysics simulation on the VIVPEH system for water fluid energy harvesting shows an electromechanical conversion efficiency is about 17.8% with the highest vibration frequency[50]. The macro fiber composite beam PEH is immersed in the vortex shed of the water. The output electric power increases with the water velocity[51].

According to the literature review, the vortex-induced vibration piezoelectric energy harvester is adopted for ocean wave energy harvesting and it is apt to convert low-frequency waves motion into high-frequency vibrations. Hence, this research will focus on the OWC ocean wave energy harvesting potential of Wave-VIVPEH to demonstrate an effective method and improve the output power of microscale electric generators. In this paper, the piezoelectric energy convertor is substituted for a conventional Faraday's law electromagnetic induction power generator that is coupled with air in the vent tunnel. The novel ocean wave harvester combines the fundamental fluid mechanics of pneumatic and hydraulic pressure in the OWC air chamber and the vortex-induced vibration in the vent tunnel. For future applications, it is desirable to supply sufficient electric power within a limited small space of the intelligent buoy that is spread all over

the ocean surface.

This article elaborated on the research work that is organized as follows. The Wave-VIVPEH physical model and theoretical simulation of energy fluxes are formulated in section 2 where the innovative idea and the mathematical theory predict the energy harvesting responses. In section 3, the air performance in the chamber is investigated and compared with the numerical wave flume simulation. In section 4, the airflow vortex-induced vibration is provided to present Wave-VIVPEH in the vent tunnel. In section 5, the experiments are performed on wave energy harvesting with a wave flume and VIV piezoelectric conversion in a wind tunnel to identify the theoretical model and validate the prediction performance of the proposed Wave-VIVPEH model. Finally, the main work is concluded and some perspectives are presented in section 6.

2 Mathematical and simulation model

2.1 Physical model and theoretical simulation of energy fluxes

The schematic of a conventional ocean Wave-VIVPEH consists of an air chamber and a vent tunnel as shown in Fig.1. A bluff body and a piezoelectric cantilever beam energy harvester are fixed respectively in the tunnel to convert the airflow kinetic energy into electric energy. The air chamber is a semi-submersible structure that is embedded in the intelligent buoy to collect ocean waves. As the incident waves flow in and out of the air chamber, the free water surface oscillates up and down. Subsequently, the relative oscillating pressure is induced that pushes air flow in the chamber through the vent tunnel as shown in Fig.1(a) and (b). Ultimately, the vortex shedding occurs downstream of the cylindrical bluff body as shown in Fig.1(c) and (d). The piezoelectric cantilever beam is settled in the wake region and its vibrations are induced by the vortex street effect. The parameters of the OWC air chamber and the simulation model are shown in Fig.1. The properties and parameters of Wave-VIVPEH are detailed in Table 1, which are required in the theory and finite element analysis models.

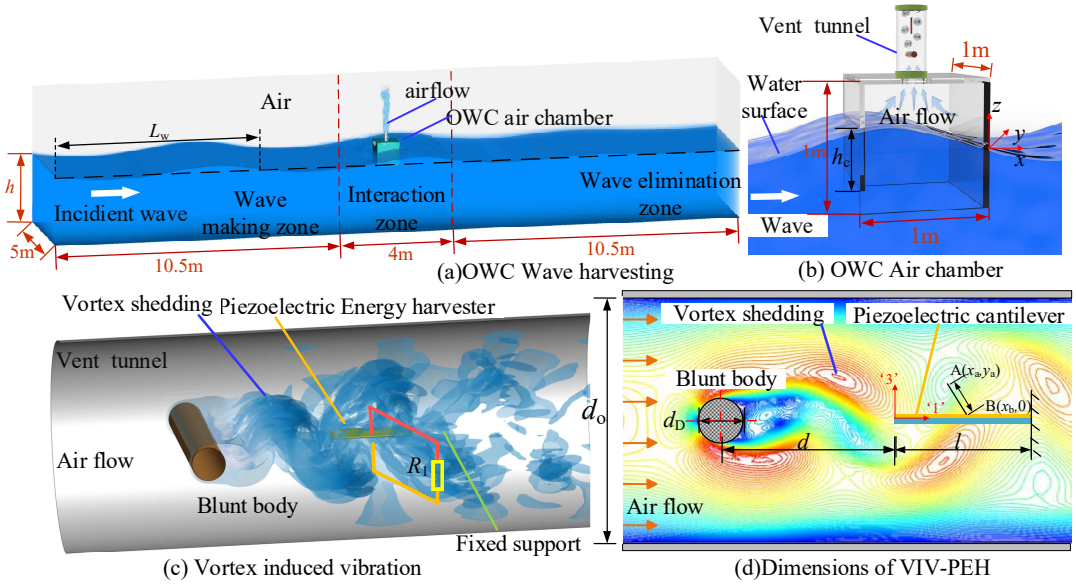

Fig.1 The schematic of the Ocean Wave VIV-PEH

Table 1 Parameters of the piezoelectric energy converter

Characteristics	Variables	PZT-5H	Substrate (Phosphor bronze)

Young's modulus (Gpa)	E_p/ E_m	56	104
Dielectric constant	ε_0	3200	
Piezoelectric voltage constant(10^{-3}Vm/N)	g_{31}	8.4	
Capacitance(nF)	C_p	136.9	
Thickness(mm)	h_p/h_m	0.5	0.5
Length(mm)	L	60	60
Width(mm)	W	30	30

The numerical modeling process of different physical domains and preliminary investigation problems are identified in Fig.2. The ocean Wave-VIVPEH energy conversion for an intelligent buoy generally consists of three stages. In the primary stage, the kinetic ocean wave is translated into pneumatic energy in the OWC air chamber. The reasonably sophisticated OWC wave energy conversion method is introduced to the theoretical descriptive models concerning the functionality and practicality of the concept. The secondary dynamic conversion stage takes place in the vent tunnel where the air flows through the blunt body and forms vortex motion as shown in Fig.1c. The vortex's exciting force on the piezoelectric body interrelates the specific power take-off (PTO) of the wave energy. The tertiary conversion stage simulates the electric power from the PEH. The theoretical analysis models possibly reveal the energy harvesting abilities of the incorporation of physical phenomena relevant to the hydrodynamic-aerodynamic coupling, vortex-induced vibration, and piezoelectric effect for the energy exchange.

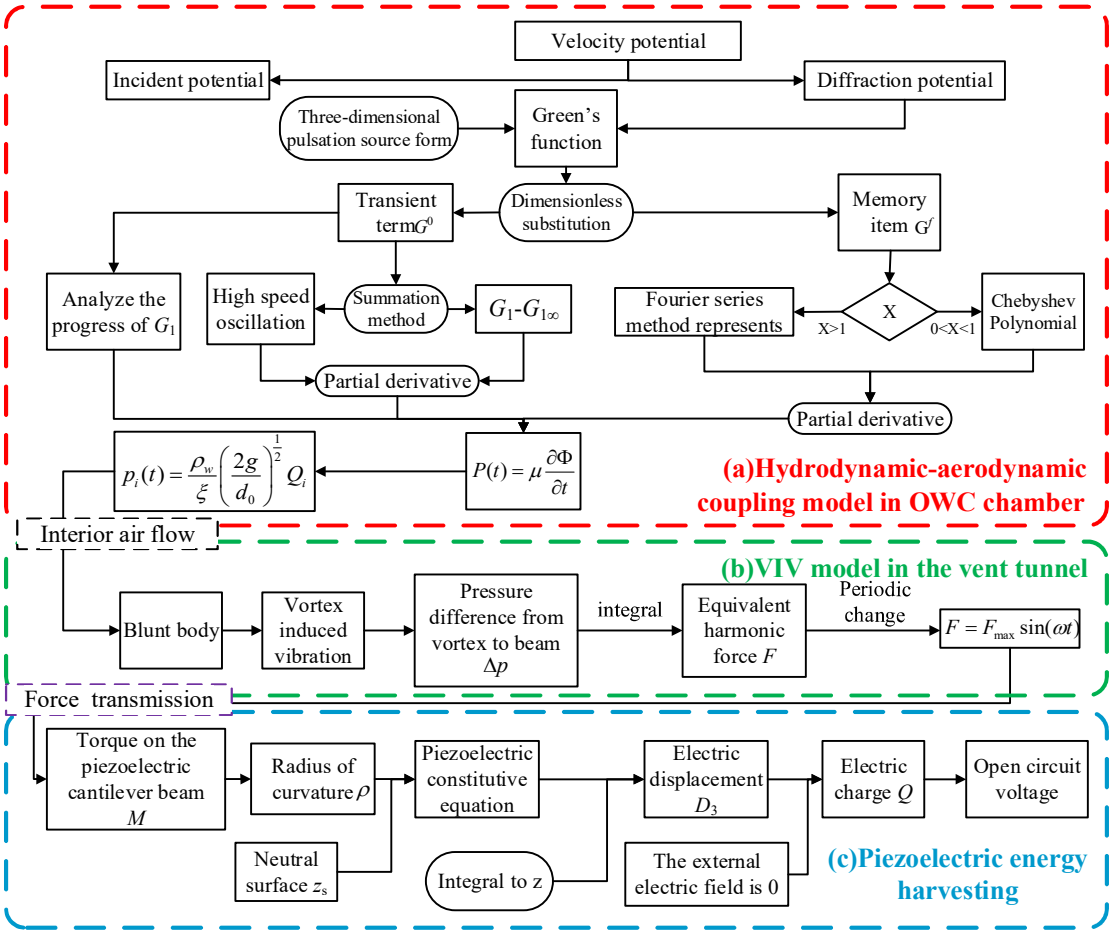

Fig.2 Schematic of the hydrodynamic-aerodynamic theoretical model and Wave-VIVPEH energy fluxes

2.2 Theoretical model of OWC air chamber

Assuming that the free water surface in the air chamber produces uniform vibration when the incident wave acts, the absorption energy by the wave energy harvester relates to the heaving motion of the OWC inside the air chamber. The control dynamic equation of the OWC wave energy harvesting device when the waves move forward sinusoidally by their complex amplitudes[52]

$$(m_0 + \rho S_a \Delta h_c)\ddot{h}_c(t) + (B + C_d)\dot{h}_c(t) + C_w h(t) = F e^{-i\omega t} \tag{1}$$

where m_0 is the mass of the water column in the chamber without oscillation; and Δh is the difference of height between the OWC free surface and ocean water surface of the outside chamber; ρ is the density of water; S_a is the inner and horizontal cross-sectional area of the chamber; $\ddot{h}_c(t)$, $\dot{h}_c(t)$, $h_c(t)$ are respectively the acceleration, velocity, and displacement of the OWC to time t in the vertical direction; B is the hydrodynamic coefficients and C_d is the damping coefficient of the air chamber when the water column and the air change; C_w is the restoring coefficient attributed to hydrostatic pressure; $Fe^{-i\omega t}$ is the exciting force caused by incident waves, which is related to incident potential and reflection potential; ω is the oscillating frequencies, that equals to the wave frequency, $\omega=2\pi/T$ and T is the wave period; i is the imaginary unit.

The subject of this study assumes the small-amplitude wave as an ideal fluid, that is incompressible, irrotational, uniform, inviscid, and ignores surface tension. The hydrodynamic motions of the OWC inside the air chamber are simulated with the linear potential flow method and the fluid continuity equation. For a semi-submersible body with an object surface of $S(x, y, z) = 0$, the velocity potential Φ in the flow field can be solved by the vector identity $\nabla^2\Phi \equiv 0$ for any scalar function and the velocity vector is defined as Eq.2 which is a complex spatial velocity potential independent of time (t) and suitable for the Laplace equation[40]. Cartesian coordinates are shown in Fig.1b and the origin is at the back wall. The horizontal origin of xy place is at the free surface and x-axis along with the forward motion of wave the z-axis in vertically upwards.

$$\left.\begin{aligned} \vec{v} &= \nabla\Phi(x, y, z, t) \\ \nabla &= [\frac{\partial}{\partial x}, \frac{\partial}{\partial y}, \frac{\partial}{\partial z}]' \end{aligned}\right\} \tag{2}$$

where $\vec{v}$ is the velocity vector of the seawater. Φ is described by its corresponding complex value based on the linear small-amplitude wave theory.

$$\Phi = \mathrm{Re}[\varphi(x, y, z)e^{-i\omega t}] \tag{3}$$

where φ is the spatial velocity potential function.

The velocity potential theory is utilized to solve the motions of OWC and the aerodynamic performance in the air chamber. The various items appearing in these step-by-step processes can be grouped into two parts: (1) the incident and scattering velocity potential and (2) the Green function solved method. The program is divided into several modules. The schematic diagram of the numerical model development is shown in Fig.2a. The time history of air pressure motions for particular wave frequencies is given with numerical simulation in the following section.

The OWC wave energy harvesting device is regarded as a three-dimensional (3D) semi-submersible box. To solute the velocity potential function, the fluid domain of seawater

around the air chamber is divided into three regions: the inner region enclosed by the wall of the chamber, the outside region, and the interface region between the aforementioned areas, which is adapted for the continuous conditions of pressure and velocity[53].

According to the principle of linear superposition, the ideal fluid moves forward with wave motion from time t=0. After a finite time, the velocity potential Φ in the regular linear small wave flow field is decomposed into the incident velocity potential Φ_i and the scattering velocity potential Φ_s.

$$\Phi(x,t) = \Phi_i(x,t) + \Phi_s\left(x,t\right) \tag{4}$$

The water is considered finite depth. When the ocean wave enters the OWC chamber the incident velocity potential can be expressed as[54]

$$\Phi_i = \frac{gH_a}{\omega}\frac{\cosh k(z+h)}{\cosh kh}\sin(kx\cos\beta + ky\sin\beta - \omega t) \tag{5}$$

where g is the acceleration of gravity; H_a is the wave amplitude, h is the water depth; k is the wavenumber of the incident wave that is related to the wavelength L_w, k=2π/L_w; and β is the incident wave's direction angle.

The scattering velocity potential is generated by the diffraction velocity potential and the radiation velocity potential, which generate from the incident wave. According to the definite solution condition, the Green function method can be calculated by the three-dimensional(3D) Green function method[55-57].

$$\Phi_s = \iint_{S_w} \sigma_s G(P,Q)ds \tag{6}$$

where $G(P,Q)$ is the green function; $P(x,y,z)$ is the source point; $Q(x_0,y_0,z_0)$ is the domain point; S_w is the boundary surface of the water in the air chamber; σ_s is the source strength of the 3D pulsation source, which is solved with the discretization numerical method based on the second type of Fredholm equation as follow:

$$-2\pi\sigma_s + \iint_{S_w} \sigma_s \frac{\partial G(P,Q)}{\partial x}ds = -\frac{\partial \Phi_s}{\partial x} \tag{7}$$

The velocity potential is solved with Green's function with the finite-depth of seawater[55] For convenience, the derivations of Green's function are in Appendix A

Green's function G is constructed at the ocean surface. The ocean waves behave according to the theory equation, which can be written a representation for the velocity function Φ(x, y, z; t) in items of initial conditions and its normal derivatives on the wave surfaces. The wave motion is described by the velocity potential of the free surface particles and the immersed water domain around the air chamber. In all time domains, the resulting pulsating pressure on the free wave surface is then mathematically derived from the velocity potential that combines the incident and scattering velocity potential. The pressure of the air chamber can be expressed as.

$$P(t) = \zeta_o \frac{\partial \Phi}{\partial t} = \zeta_o \frac{\partial(\Phi_i + \Phi_s)}{\partial t} \tag{8}$$

where ζ_0 is the damping coefficient of the oscillating motion in the air chamber.

The OWC and the air chamber are capable of extracting the mechanical kinetic energy from the waves incident upon the floating buoy. With the OWC moving up and down, it is assumed that the air column compresses adiabatically and the airflow is ideal incompressible with the variation of the mass of this column due to air movement through the orifice of the air chamber. The OWC

drives the air flowing through the vent tunnel. When the sea waves rush into the air chamber they cause the volumetric compression of the air in the chamber, and the airflow Q_i at the orifice of the air chamber is proportional to the air pressure $P(t)$[58].

$$p(t) = \frac{\rho_a}{\xi_a}\left(\frac{2g}{d_0}\right)^{\frac{1}{2}} Q_i \tag{9}$$

where ρ_a is the air density, ξ_a is the air damping coefficient, d_0 is the orifice diameter of the air chamber.

The volume change of the air chamber is expected to affect fluid velocity. The variation can be determined by the relationship between the velocity v of the air chamber and the airflow Q_i.

$$Q_i = v_c A_c = \frac{\pi d_0^{\,2}}{4} v \tag{10}$$

where v is the air velocity at the orifice of the chamber; A_c is the cross-section area of the orifice.

2.2 Theoretical model of vortex exciting force on the PEH

Normally, the ocean wave's frequencies are ultralow(≈1Hz) which impedes the improvement of the piezoelectric energy harvesting effect. It is very hard to achieve a resonant that only mechanically tunes the intrinsic frequency of PEH to match the ocean wave frequency. To address this issue, the vortex-induced vibration is applied in the vent tunnel that connects with the orifice of the air chamber. When the buoy heaves with the ocean waves, the oscillating water column in the air chamber induces low frequency and high-speed airflow into the vent tunnel. Furthermore, the high-frequency air vortex sheddings downstream of the bluff body and then provoke the piezoelectric cantilever beam deformation, as shown in Fig.1(c). One end of the piezoelectric cantilever beam is clamped and the free end of it can vibrate with the vortex shedding in the wake flow field.

When ocean waves enter the air chamber periodically, the blunt body performs and stimulates the air vortex at a higher frequency that is described as[59].

$$f = S_t \times v / d_D \tag{11}$$

where d_D is the diameter of the bluff body, and S_t is the Strouhal number that is determined by Reynolds number R_e as follows.

$$R_e = d_D (v / \mu_{air}) \tag{12}$$

Where μ_{air} is the kinematic viscosity of the air.

Both sides of the piezoelectric cantilever beam surfaces are alternately forced by the vortex street sheddings. Thereout, the differential pressure between vortex core A (x_a, y_a) and B(x_b, 0) on the cantilever beam generates a force loading on the piezoelectric beam as shown in Fig.1(d). The distance from A to B is r_{ab}.

$$r_{ab} = \sqrt{(x_b - x_a)^2 + y_a^{\,2}} \tag{13}$$

Further, the pressure difference Δp is described[60].

$$\Delta p = \frac{\rho_a}{2}\left(\frac{v_0 \Gamma}{\pi r_{ab}} - \frac{\Gamma^2}{4\pi^2 r_{ab}^2}\right) \tag{14}$$

where v_0 is the average horizontal velocity at the center of the vortex, which approximates the fluid velocity v. The strength of the vortex can be expressed by the velocity circulation Γ as[61].

$$\Gamma = \Gamma_0 \left(1 - e^{-\left(r_0^2 / 4\mu_{\text{air}} t \right)} \right) \tag{15}$$

where Γ_0 is the initial vortex intensity[62], $\Gamma_0 = v d_{\text{D}} / 2S_t$.

Hence, the amplitude of the instantaneous vortex exciting force on the piezoelectric cantilever beam is expressed as an integral of the intensity over the surface.

$$F = \int_0^{l_{\text{p}}} \Delta p \times b_{\text{p}} dx = \frac{1}{2} \rho_{\text{a}} b_{\text{p}} \int_0^{l_{\text{p}}} \left(\frac{v_0 \Gamma}{\pi r_{\text{ab}}} - \frac{\Gamma^2}{4\pi^2 r_{\text{ab}}^{\ 2}} \right) dx \tag{16}$$

where l_{p} and b_{p} are the length and width of the piezoelectric cantilever beam, respectively.

When the vortexes shed stably, the ordinate of vortex center position is given as y_{a}=1.3d_{D} /2. Furthermore, when the shedding arrives at the middle of the beam x_{a}= l_{p}/2, the exciting force amplitude is maximal which is described as follows.

$$F_{\max} = \frac{1}{2} \rho_{\text{a}} b_{\text{p}} \int_0^{l_{\text{p}}} \left\{ \frac{v_0 \Gamma}{\pi \sqrt{\left(x - \frac{l_{\text{p}}}{2} \right)^2 - \left(\frac{1.3 d_D}{2} \right)^2}} - \frac{\Gamma^2}{4\pi^2 \left[\left(x - \frac{l_{\text{p}}}{2} \right)^2 - \left(\frac{1.3 d_D}{2} \right)^2 \right]} \right\} dx \tag{17}$$

When the periodic vortex sheddings in the near wake move flip-flopped on the surface of the piezoelectric cantilever beam in turn they yield the equivalent harmonic force. For a steady-state amplitude solution in Eq.17, the cyclic exciting force load is given as follows.

$$F = F_{\max} \sin(2\pi f t) \tag{18}$$

2.3 Theoretical model of cantilever beam PEH

The piezoelectric energy harvesting technologies have gained considerable attention in the self-powered sources of wireless sensor nodes. The piezoelectric cantilever beam has been chosen as the basis converter for vibration energy harvesting rather than a stack because of the attainable higher strain. It consists of a piezoelectric layer and an elastic metal substrate to improve the strength, as shown in Fig.1(c). Based on the piezoelectric material properties on the cantilever beam, the mechanical and electrical quantities are coupled in the d_{31} direction which has higher piezoelectric sensitivity and the average strain. The output electric power is related to the electromechanical coupling factor. According to the elastic theory of materials, the constitutive relationship between stress and dielectric displacement of the piezoelectric layer is[63]:

$$\begin{cases} T_{\text{p}} = E_{\text{p}} (S_1 - g_{31} D_3) \\ E_3 = -g_{31} T_{\text{p}} + \beta_{33}^{\text{T}} D_3 \end{cases} \tag{19}$$

where S_1 is the strain in the "1" direction, which can be expressed as S_1, T_{p} is the stress in the "1" direction induced by the combined mechanical and electrical effects, g_{31} is the constant of piezoelectric voltage, and E_{p} is the Young's of the piezoelectric material modulus, D_3 and E_3 are the force of electric displacement and electric field in the "3" direction, respectively. $\beta_{33}^T = 1 / \varepsilon_{33}^T$ is the rate of dielectric isolation, $\varepsilon_{33}^T = 1300 \varepsilon_0$ is the dielectric constant or permittivity of the piezoelectric layer.

Because it has different values of Young's modulus on the piezoelectric layer and the elastic

substrate, the distance from the upper to the neutral surface of the composite beam can be given according to the Euler-Bernoulli method[64].

$$z_{\mathrm{s}}=\frac{E_{\mathrm{p}}\frac{h_{\mathrm{p}}{}^{2}}{2}+E_{\mathrm{m}}h_{\mathrm{m}}(h_{\mathrm{p}}+\frac{h_{\mathrm{m}}}{2})}{E_{\mathrm{p}}h_{\mathrm{p}}+E_{\mathrm{m}}h_{\mathrm{m}}} \tag{20}$$

where E_{m} is Young's modulus of the metal elastic substrate. h_{m}, h_{p} is the thickness of the substrate and the piezoelectric layer, respectively.

When the piezoelectric cantilever is subjected to external exciting force, the moment is integral over the surface.

$$M_{\mathrm{z}}=\int_{0}^{b_{\mathrm{p}}}\int_{z_{\mathrm{s}}-h_{\mathrm{p}}}^{z_{\mathrm{s}}}zT_{\mathrm{p}}dydz+\int_{0}^{b_{\mathrm{p}}}\int_{-h+z_{\mathrm{s}}}^{z_{\mathrm{s}}-h_{\mathrm{p}}}zT_{\mathrm{m}}dydz=(x-l_{\mathrm{p}})F \tag{21}$$

where T_{m} is the stress in the 1 direction of the metal substrate, that is $T_{\mathrm{m}}=E_{\mathrm{m}}S_1$.

Hence, the curvature ρ_{b} of the piezoelectric cantilever beam can be obtained by Eq.21 with the exciting force and electric field.

$$\rho_{\mathrm{b}}=-\frac{6}{\Lambda_1 E_{\mathrm{p}}b_{\mathrm{p}}h^{3}}\left[\frac{2(h_{\mathrm{p}}+h_{\mathrm{m}}\beta)(x-l_{\mathrm{p}})F}{h_{\mathrm{b}}}+h_{\mathrm{m}}h_{\mathrm{p}}\beta g_{31}E_{p}D_3\right] \tag{22}$$

where h_{b} is the thickness of the composite piezoelectric cantilever beam, and Λ_1 is the simple code symbol as follows.

$$\Lambda_1=\frac{h_{\mathrm{m}}^{4}(1-\beta)^{2}}{h_{\mathrm{b}}^{4}}-\frac{(4h_{\mathrm{m}}^{3}-6h_{\mathrm{m}}^{2}h+4h^{2}h_{\mathrm{m}})(1-\beta)}{h_{\mathrm{b}}^{3}}+1 \tag{23}$$

The curvature Eq.22 is substituted into Eq.19 with the equivalent harmonic force of Eq.18. Thus, the electric field E_3 is obtained simultaneously. And the voltage on the opposing surfaces of the piezoelectric layer is calculated with an integral.

$$V=\int_{z_{\mathrm{s}}-h_{\mathrm{p}}}^{z_{\mathrm{s}}}E_3dz=\frac{h_{\mathrm{p}}}{\Lambda_1 b_{\mathrm{p}}h_{\mathrm{b}}}\left[\frac{6h_{\mathrm{m}}\beta g_{31}(l_{\mathrm{p}}-x)F}{h_{\mathrm{p}}}+\frac{\Lambda_2 b_{\mathrm{p}}h_{\mathrm{b}}^{3}\beta_{33}^{\mathrm{T}}D_3}{h_{\mathrm{p}}+h_{\mathrm{m}}\beta}\right] \tag{24}$$

where $k_{31}^{2}=E_{p}g_{31}^{2}/\beta_{33}^{T}$, and Λ_2 is a new code symbol as follows.

$$\Lambda_2=\frac{\Lambda_1(h_{\mathrm{p}}+h_{\mathrm{m}}\beta)(1+k_{31}^{2})}{h_{\mathrm{b}}}-\frac{3h_{\mathrm{m}}^{2}h_{\mathrm{p}}\beta^{2}k_{31}^{2}}{h_{\mathrm{b}}^{3}} \tag{25}$$

The electric displacement D_3 can be obtained by rewriting the voltage Eq.24.

$$D_3=\frac{h_p+h_m\beta}{h_p\beta_{33}^{T}\Lambda_2 b_{\mathrm{p}}h_{\mathrm{b}}^{2}}\left[\frac{6h_m h_p\beta g_{31}(x-l_{\mathrm{p}})F}{h_{\mathrm{b}}^{2}}+\Lambda_1 h_{\mathrm{b}}b_{\mathrm{p}}V\right] \tag{26}$$

Generally, the piezoelectric material is shaped as a rectangular sheet block on an elastic metal substrate. The charges on the two parallel conducting electrodes yield by integrating over the coupling area of the piezoelectric cantilever beam with electric displacement.

$$Q=\int_{0}^{b_{\mathrm{p}}}\int_{0}^{l_{\mathrm{p}}}D_3dydx=\frac{(h_p+h_m\beta)l_{\mathrm{p}}{}^{2}}{\beta_{33}^{T}\Lambda_2 h_{\mathrm{b}}^{3}}\left[\frac{-3h_m\beta g_{31}F}{h_b}+\frac{\Lambda_1 b_{\mathrm{p}}h_b^{2}V}{h_p l_{\mathrm{p}}}\right] \tag{27}$$

When an external force and an external electric field are present at the same time, the equation formula above is used. If the external electric field is zero, the charges are produced alone by the equivalent harmonic cyclic exciting force.

$$Q_{\mathrm{p}}=\frac{-3h_m\beta(h_p+h_m\beta)g_{31}l_{\mathrm{b}}^2F}{\beta_{33}^T\Lambda_2h_{\mathrm{b}}^3} \tag{28}$$

Moreover, if the cantilever is excited alone by the electric field, the capacitance of the piezoelectric cantilever is equivalent to

$$C_{\mathrm{p}}=\frac{(h_p+h_m\beta)\Lambda_1b_{\mathrm{p}}l_{\mathrm{p}}}{h_p\beta_{33}^T\Lambda_2h_{\mathrm{b}}} \tag{29}$$

The piezoelectric cantilever beam behaves as a flat-plate capacitor, for which $V_{\mathrm{oc}}= Q_{\mathrm{p}}/C_{\mathrm{p}}$. The output open-circuit voltage is available to reveal the electric energy on the converter without the loaded device.

$$V_{oc}=-\frac{3h_mh_p\beta g_{31}l_{\mathrm{p}}}{\Lambda_1b_{\mathrm{p}}\mathrm{h}_{\mathrm{b}}^3}F \tag{30}$$

According to Eq.18, the output voltage is alternating current voltage with the frequency f of the cyclic vortex exciting force loads system and the angular frequency $\omega_{\mathrm{v}}=2\pi f$. The equivalent voltage and the output electric power are given with the assumed external load resistances.

$$V_L=V_{oc}\left|\frac{R_L}{R_L+\dfrac{1}{j\omega_{\mathrm{v}}C_{\mathrm{p}}}+R_s}\right| \tag{31}$$

$$P_{\mathrm{out}}=\frac{V_{\mathrm{L}}^2}{2R_{\mathrm{L}}}=V_{oc}\left|\frac{R_{\mathrm{L}}}{2(R_{\mathrm{L}}+\dfrac{1}{j\omega_{\mathrm{v}}C_{\mathrm{p}}}+R_{\mathrm{s}})^2}\right| \tag{32}$$

where, R_{L} is the external load, and R_{s} is the equivalent internal resistance of the piezoelectric energy converters.

2.4 The wave flume OWC chamber model

The computational fluid dynamics(CFD) numerical model of three-dimensional(3D) numerical wave flume has been widely employed to evaluate the available theoretical calculation on the conversion mechanism[65-67]. The OWC and the air chamber are the pivotal primary conversion subsystems to extract the wave energy. The hydrodynamic and aerodynamic are coupled to achieve energy conversion simulation in the chamber. The experimental, analytical, and numerical methods are developed to aid the validation analysis of the hydrodynamic performance of OWC devices. The air-water two-phase interaction is simulated based on the volume of fluid (VOF) method and the Navier–Strokes equations in the CFD software[68]. The 3D model of OWC pneumatic chamber geometry is established by Solidworks modeling software on a scale of 1:1 in the numerical flume as shown in Fig.1(a). The predefined parameters of the wave energy extraction device have been given in section 2. It assumed that waves perform in steady and periodic air-flow calculation conditions. A water column oscillates up and down like a piston due to the forces of the normal incident waves. and then it pushes or inspires air through the vent tunnel of the air chamber. The numerical waves are produced by time-domain variation with specifying wave heights and lengths at the inlet of the CFD computational domain. It is well documented that the total width of the flume should be at least five times that of the chamber to

isolate the interaction impact of the sidewall[69]. Thus, the three-dimensional numerical wave flume is set up (see Fig.1) which consists of four sections: the chamber, wave, ocean water, and air in the chamber and above the surface of ocean water. The cubic OWC chamber is anchored at the water surface of the flume. The computational domain is finely divided into several regions that are (A)gas phase, (B)gas-liquid junction surface, (C) ocean water phase, (D)fluid-solid coupling domain, and (E)wave-eliminating domain (see Fig.3a). The motions of contiguous domains on the interface of two adjacent fluids are bonded with the re-meshing method of ANSYS Meshing Platform (AMP). Globally, the grid refinement and densities in the respective region are set as D>B>A&C>E to balance the calculation accuracy and computational effort. Furthermore, hybrid unstructured mesh models are used with hexahedral and tetrahedral type elements in different regions for validation and refinement analysis in order to achieve a smooth transition between the vicinity of the OWC. Formally, the mesh independence verification has been conducted according to the specification of the CFD software[70]. In the vent tunnel of the air chamber, the simulation resolutions of air are compared with a series of mesh grid sizes to check the mesh independence as shown in Fig.3c. The mesh convergence for the compressed air in the chamber was calculated from coarsest to the finest sizes (i,e. Gride size 128 mm to 32 mm). The grid size of the fluid-structure interaction zone is meshed and compared from 128 mm to 64 mm. The estimated air velocity changes by more than 17.6%. Furthermore, since the grid size decreases from 64 mm to 32 mm, the percentage difference between air velocity predictions changes by less than 1%. The optimum mesh grid sizes were refined enough by the mesh independence analysis, which has confirmed sufficient accuracy and minor computational effort comparatively.

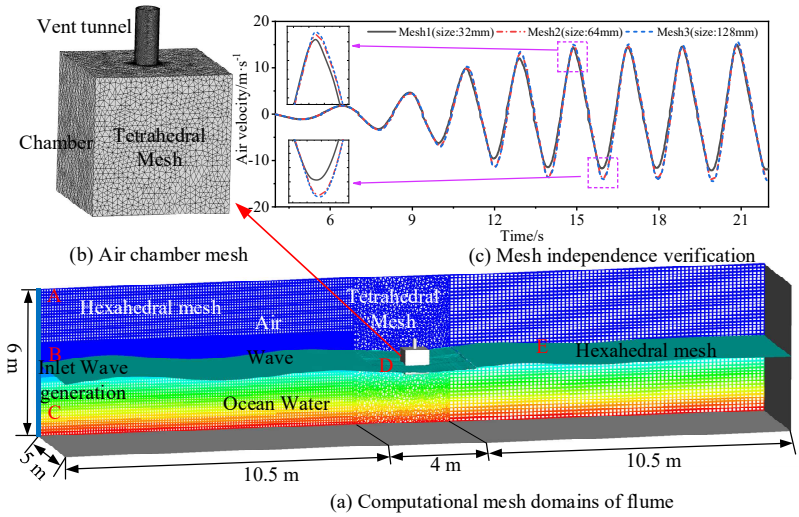

Fig.3 Mesh setup of the numerical wave flume

3. Results and discussion

3.1 Theoretical calculation of air performance in chamber

The full field scale model of the OWC chamber is used for the airflow velocity analysis of the wave energy conversion, which is capable of extracting the maximum amount of energy from the incident waves. The structure and wave parameters are chosen close to the prevailing ocean climate in the Western Pacific. Therefore the waves incident upon the air chamber and force the water column moving like a piston. To achieve a theoretical calculation of air performance in the chamber, it is assumed that the air is incompressible and adiabatical when air travels through the vent tunnel. when ocean water rushes into the chamber with the frequencies of waves, the typical

pressure and airflow velocity are calculated from the theoretical models in Eq.8 and Eq.10. The results of the time series graph of air velocity and pressure are related to the condition of wave periods (see Fig.4). The OWC chamber with the same structure(see in Fig.1) is tested under various regular waves with periods varying from 1.5 s to 3 s in the offshore of China and a constant wave height of 0.3 m, to derive air performance curve. The air velocity increase with the pressures in the chamber, especially, it is affected by the wave periods. The maximum values peak when the water column oscillates in resonance at the period of 2.5s. Therefore it can predict theoretically the resonant frequency of an OWC and the air pressure variations which provide the aerodynamic force to the vortex vibration in the vent tunnel.

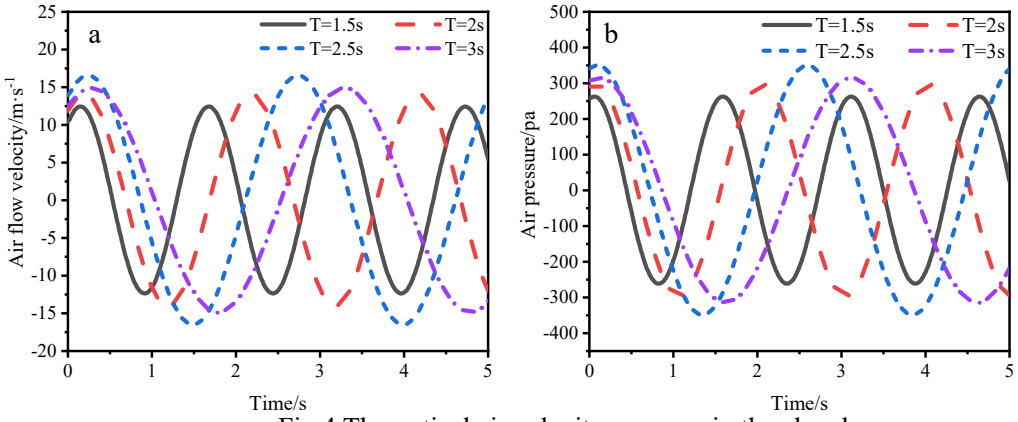

Fig.4 Theoretical air velocity pressure in the chamber

3.2 The numerical simulation of air performance

The same OWC chamber (for configuration Fig.1a) in the computational domain is modeled with the CFD method which has been illustrated in Fig.3. The numerical model can simulate the fluid properties of water and air surrounding the OWC chamber. The streamlines and velocity magnitudes for waves and air are shown in Fig.5. Thereinto, the three-dimensional flow vector cloud diagram (see Fig.1a) presents the simulation of the outwards airflow performance. The air exhalation and inhalation processes are produced during a wave cycle, as shown in Fig.5a and b, respectively. The vectors of the streamlines and velocity of the two fluid phases are plotted together when the water passes from the front wall of the chamber. The arrows in Fig.5 represent the direction of the inward and outward water. Synchronously, the volume of the air chamber is squeezed or inflated with the water column oscillating. In the vent tunnel, the vector of gradient shown in red color indicates the vertical air velocity is much greater than the inflowing water velocity. The OWC motions accelerate air through the vent tunnel to induce vortex vibration.

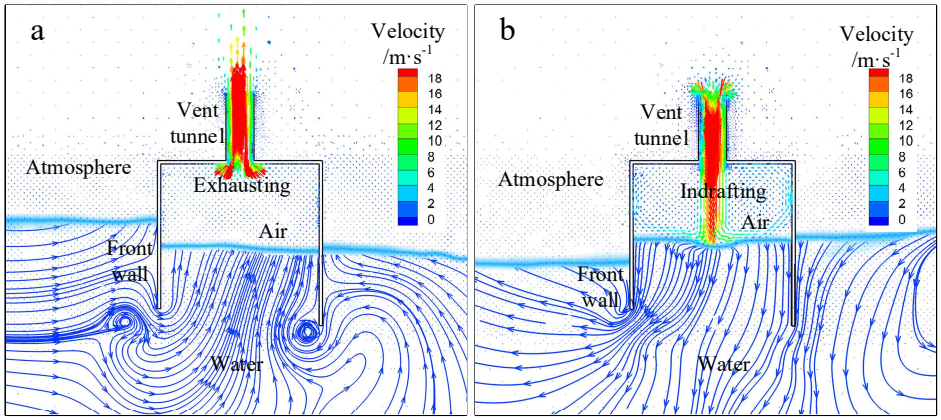

Fig.5 Streamlines and velocity vector of water and air

The visualized propagating wave passes the front wall during a wave cycle. The air velocities and pressure vary with the different locations of the water surface. The vector diagrams of velocity are present as the time evolution of the airflow in a wave period (see Fig.6) when the two fluids flow in and out of the pneumatic chamber instantly. In the first quarter of the wave period (0-*T*/4), the incident wave crest arrives in front of the chamber raising the inner water column level constantly and accelerating the air exhaling until the wave falls back to the free surface of the ocean water as shown in Fig.6a-d. Nacheinander, the water descends downward from the free surface of the ocean when the wave trough arrives in the second half-cycle. Therefore, the water column drops down and the negative pressure inside the chamber induces the air to flow through the vent tunnel in the opposite direction as shown in Fig.6e-h.

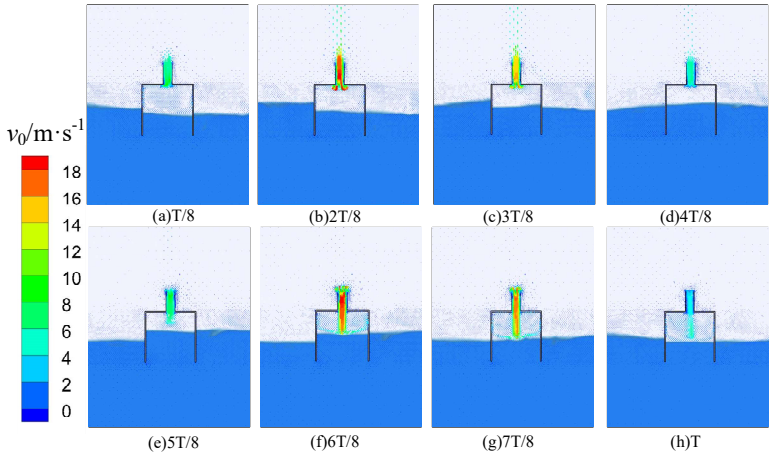

Fig. 6 Velocity vector of the airflow in the vent tunnel

The simulation monitors distribute at various points that automatically collect the wave motion and pneumatic energy passing the vent. The regular waves perform with a static wavemaker at the left inlet boundary of the computational domain based on the validated RANS CFD models as shown in Fig.3, and the ocean water depth is set to 3 m and the front wall submerges water of 0.3 m[70]. An entire time series of free wave surface elevation is analyzed in Fig.7a. Due to the unsteady behavior in the initial moment, the waves are fully developed after five cycles. Furthermore, the inner wave height rises and falls with the incident waves. A series of wave heights vary from 0.01 to 0.15 m when the wave periods change in the range of 1.5~3 s as shown in Fig.7b.

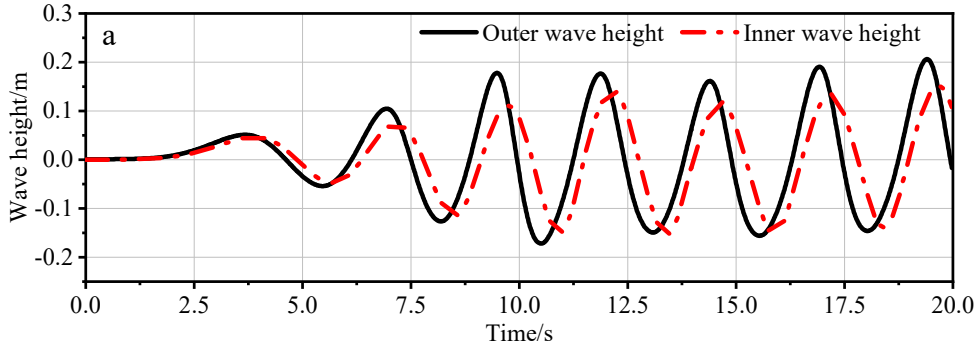

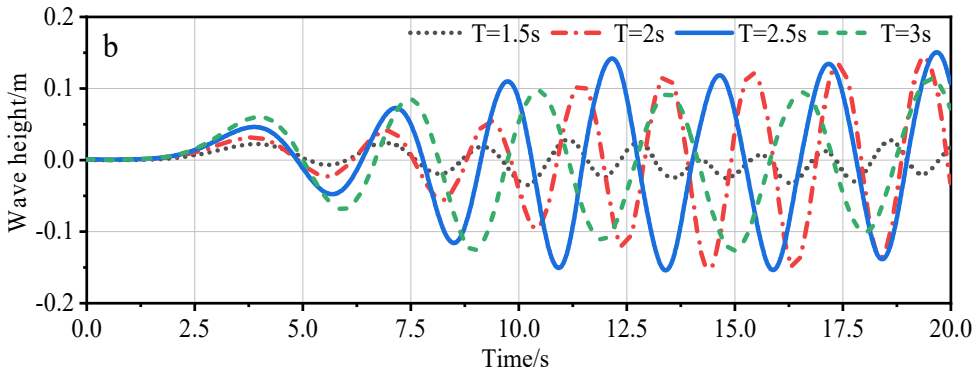

Fig.7 The time history of the wave height inside and outside the air chamber is at h_f=0.3 and d_o=0.15 m

On the other hand, the air performance inside the chamber originates from the water surface elevation. The air flux through the vent tunnel is monitored numerically with the flow velocity and pressure as shown in Fig.8. The time history curves change in accord with the oscillation of OWC as the wave periods. Based on the sizes of the air chamber in Fig.1, the maximum corresponding values occur at the wave period of T=2.5 s due to the OWC resonance with the incident wave in the pneumatic chamber. Comparisons for the peak pressure values at the positive and negative points with 336.16 Pa and -382.55 Pa respectively represent the difference between the exhalation and inhalation pressure that have been recorded in Fig.5.

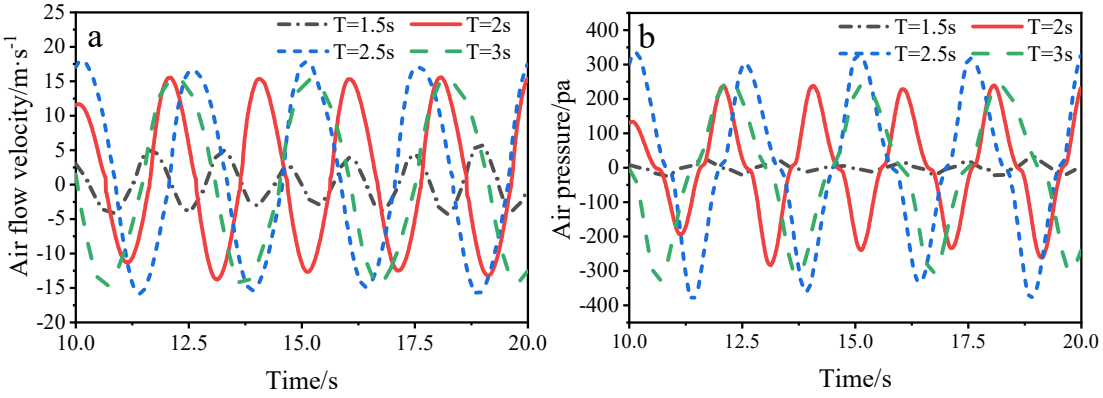

Fig.8 The air speed and pressure relate to wave periods

3.3 Validation

To validate the computational model, the air flow characteristics inside the OWC chamber are calculated to compare the theoretical results with numerical and experimental ones, respectively. In this section, the parameters are simulated and reproduced with the speeds and pressures. The aerodynamic characteristics are determined by theoretical Eq.10 and the pressure Eq.8. The simulation values are analyzed from the wave flume OWC chamber model in Fig.3. The surface water oscillates closely to the resonant frequency of the wave energy device. The comparison of the speeds and pressure results of the theoretical models agreed very well with the numerical results as shown in Fig.9. In conclusion, the theory and CFD numerical models adequately describe the performance of the water and airflow inside the OWC chamber. The aforementioned methods also provide the opportunity to address the inward or outward flow field air exchange between the atmosphere and the chamber through the vent tunnel.

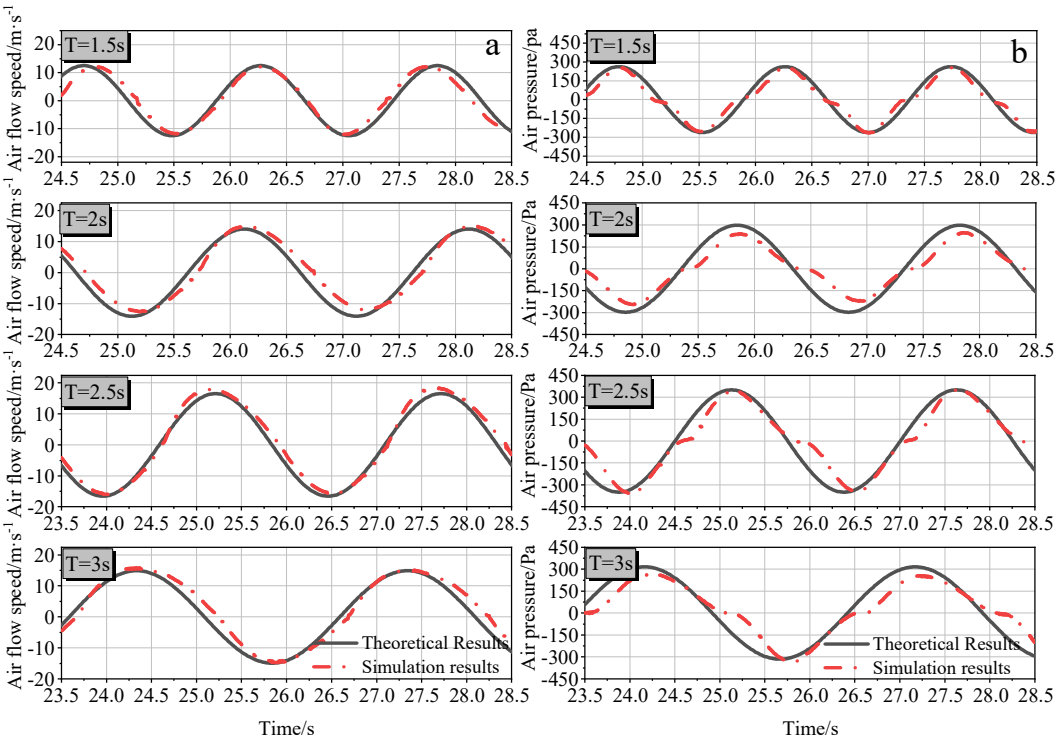

(a) airflow velocity outward and (b) pressure time series

Fig.9 Theory and CFD numerical results of air performance inside the chamber

3.4 Effects on the parameterization of the OWC chamber

In a validated simulation scenario, the optimization analysis of the waves and air dynamics in the OWC chamber model is carried out with the ocean climate states. The air flows through the vent with the pressure varying inside the enclosed chamber. These values are used for further analysis of the relative air pressure and the air velocity inside the chamber as demonstrated in Fig. 4a and b respectively. The draft of the front wall change from 0.3 to 0.5m, and the draft of the rear wall immerses from 0.5 to 0.7 m which is deeper than the front wall to enhance the water column upward in the chamber. The air velocity is the pivotal variable that determines the efficiency of the VIV PEH device in the vent tunnel. Fig.10a shows how the air pressure varies with draft depth. In the gradient graph, the small discrepancies are a result of the pressure on the front wall which only dissipates a little wave energy. Oppositely, the rear wall prompts the air pressure variation as it induces the wave to climb on the wall. The pressure initially increases with increasing dimensionless wave number parameters until resonance occurs[67]. The behavior of the airflow is influenced approximatively by the chamber pressure as shown in Fig.10b. It may be due to the effective relatedness of the water column oscillations. The vent tunnel with a bluff body is placed in the orifice of the OWC chamber model for the vortex-induced vibration.

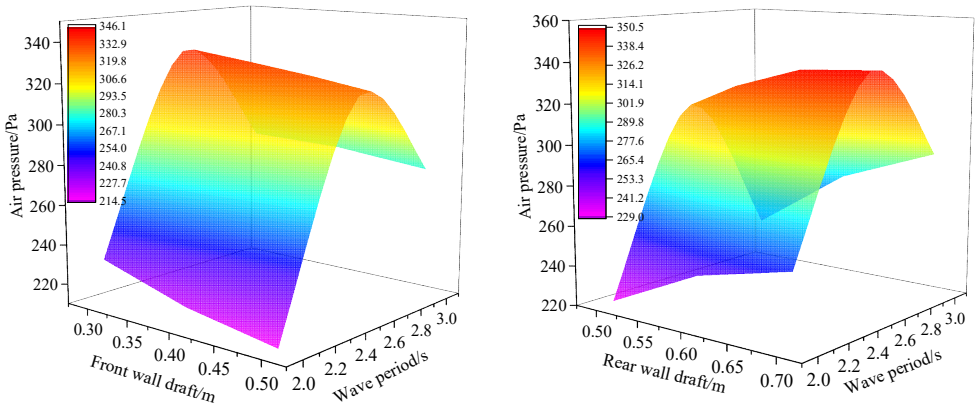

(a) Air pressure amplitudes in the chamber

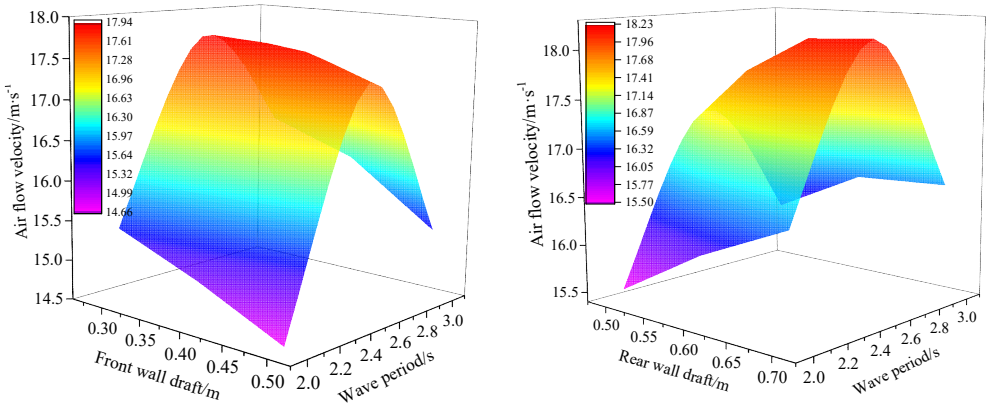

(b) Airflow velocity amplitudes at the orifice

Fig.10 The influence of chamber wall draft depth on airflow performance

4. Vortex induced vibration for PEH

4.1 Frequency of VIV

Globally, the air pressure in the pneumatic chamber fluctuates with the oscillations of the water column that compresses and expands the air volume as a piston. Therewith, the air flow triggers a power take-off (PTO) to extract the wave energy into electricity through a piezoelectric energy generator. The spectrum of air pressure is determined by the influx of waves. Furthermore, to evaluate the numerical results once more, the comparison of the frequency spectra inside the OWC chamber is extracted from this value through fast Fourier transforms as shown in Fig.11a. The theoretical air pressure responses of the three case periods to the regular incident ocean waves are well agreed with the CFD numerical model. The initial air pressure fluctuation is caused by the ocean wave motion usually in low and broad frequencies. The frequency-up conversion system can tremendously improve the energy harvesting efficiency in the higher resonance frequency[38]. Since a periodic airflow appears in the vent tunnel, a vortex-induced vibration (VIV) has been a surge of activity wakes regarding the bluff body. Henceforth, the periodic vortices are shed from a bluff body in the incoming flow from the orifice of the pneumatic chamber. Thus, the shedding vortices induce periodic forcing and cause significant oscillations at 178 Hz which is 445 times higher than the primary air pressure as shown in Fig 11b.

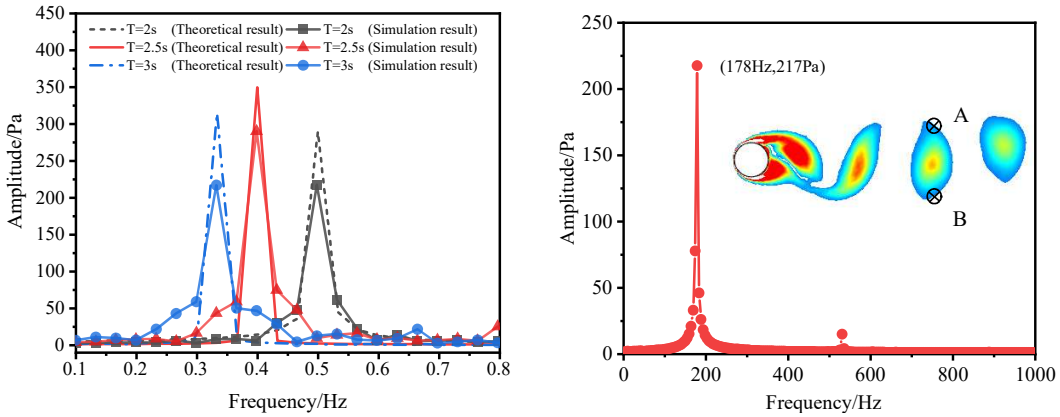

(a) Spectra at the orifice of the chamber (b) Spectra near wake regime

Fig. 11 Comparison of air pressure oscillating spectra between upstream and downstream the bluff body

The conventional piezoelectric cantilever beam is employed to harvest the airflow kinetic energy in the vent tunnel of the OWC chamber as shown in Fig.1b and c. The material and structure parameters are listed in table 1. The piezoelectric material of PZT-5H has a high electromechanical coupling coefficient that is usually bonded on the Phosphor bronze metal substrate. Thus the elastic composite beam can endure long-time alternating fatigue load and withstand large deformation. The maximum electric power is usually generated at the resonance frequency of the PEH. The structure finite element analysis model (in ANSYS 15.0 software) accurately predicts its first and second natural frequencies at 172 Hz and 1072 Hz, as shown in Fig.12. The former is close to the vortex shedding frequency of 178 Hz in the vent tunnel when the wind speed is up to 17.0 m/s downward the bluff body with a diameter of 25 mm as shown in Fig.11b.

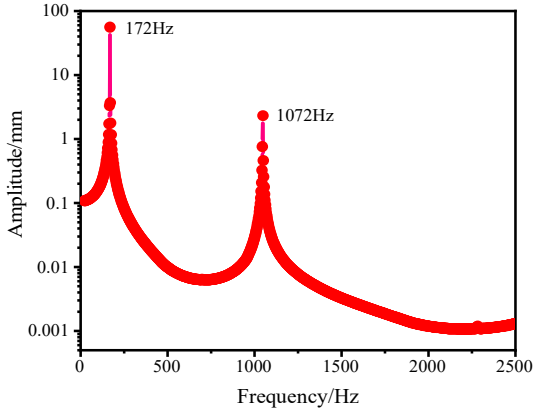

Fig.12 Inherent frequency of PEH

4.2 Power generation of VIV

Research literature has investigated the VIV vortices on the cantilever beam. However, the fluid-solid-electric physical field coupling model on the piezoelectric energy harvester has received less attention. The simulation process is relatively immature. Therefore, the multiphysics fluid-solid-electric coupled hydroelectricity system is used to illuminate the VIV interaction performance of the air fluidic field and the elastic piezoelectric composite beam with full-size coupled physical fields as shown in Fig.13(a).

The vortex shedding from the cylinder surface acts as a vibration source. To reveal the position effect in the VIV wake for the energy harvester, the span adjustment between the bluff

body and the free end of the piezoelectric cantilever beam is described with the dimensionless parameter of d/d_D that is set from 2~6. In the exhalation process of the first half of the wave cycle, as shown in Fig.13, vortices travel downstream of the bluff body. And then, the strong vortex approaches one side surface of the beam, meanwhile, a weak vortex adheres closely to the other side. In consequence, the differential pressure forces the cantilever to bend as shown in Fig.13b which respectively illustrates the pressure gradient diagram and contour diagram at the exhalation air time history of 0.75s.

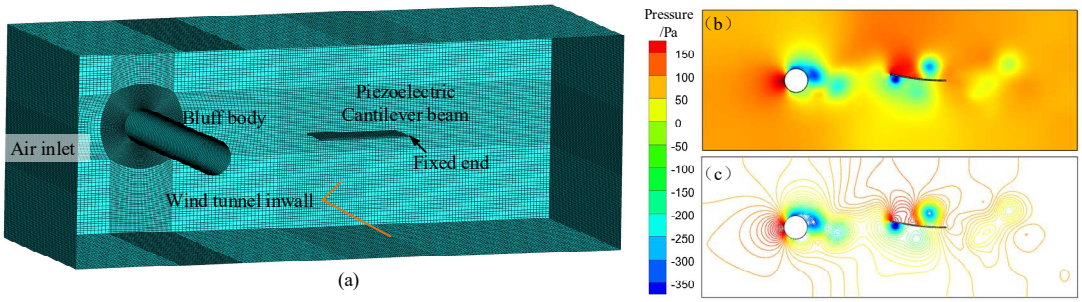

Fig.13 3D fluid-solid-piezoelectric coupling simulation (a) model (b) air pressure gradient and(c) contour diagram on the piezoelectric cantilever beam at t=0.75 s

The piezoelectric vibration is relevant primarily to the vortex-shedding period in comparison with over a large ocean wave period. The various instabilities and flow regimes of the vorticity cloud diagram are shown in Fig.14 with successive various moments which involve the development of vortex shedding in the wake. Although the roughness, turbulence levels, cylinder aspect ratio and blockage all affect the transitions, the vortex formation is often invoked in subsequent studies for the piezoelectric cantilever beam generator. The vorticity circulation profile of the vortex shedding indicates the specific location of the vortex. A pair of recirculation regions behind the bluff body in the low Reynolds numbers as shown in Fig.14a, vortices are alternately generated on both sides of the bluff body. In Fig.14a, a vortex A1 as the spearhead reaches the lower surface of the piezoelectric cantilever beam which is uplifted as shown in Fig14b. Next time, the vortex A2 and others alternate pressure on the up and low surfaces of the beam as shown in Fig.14c and d.

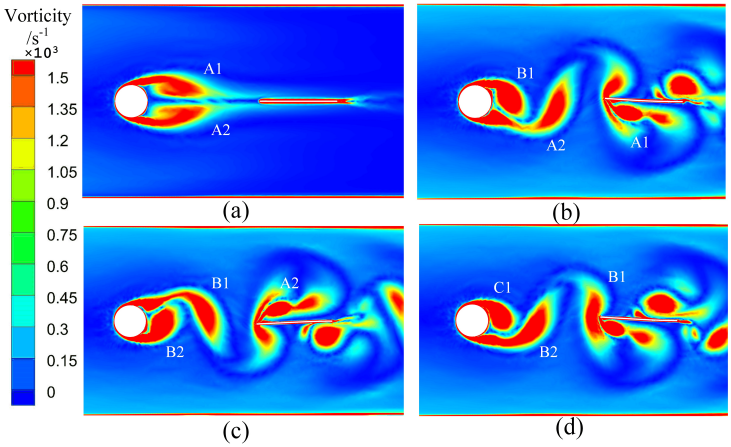

Fig.14 Vortex force on the surfaces of the piezoelectric cantilever beam

Theoretically, the airflow speed can affect the output performance of the PEH energy converter due to the intensity of vortex shedding. Fluent-Mechanical-System coupling module based on the Ansys Workbench software simulates the transform kinetic energy of air flowing into electrical energy. In the VIV wake of a bluff body, the piezoelectric cantilever beams are induced vibration with the steady wind speed to evaluate their performance as energy generators. The

assembled air speeds for VIV are stated to compute the output voltages as shown in Fig.15 which agreed well with the theoretical values by Eq.30.

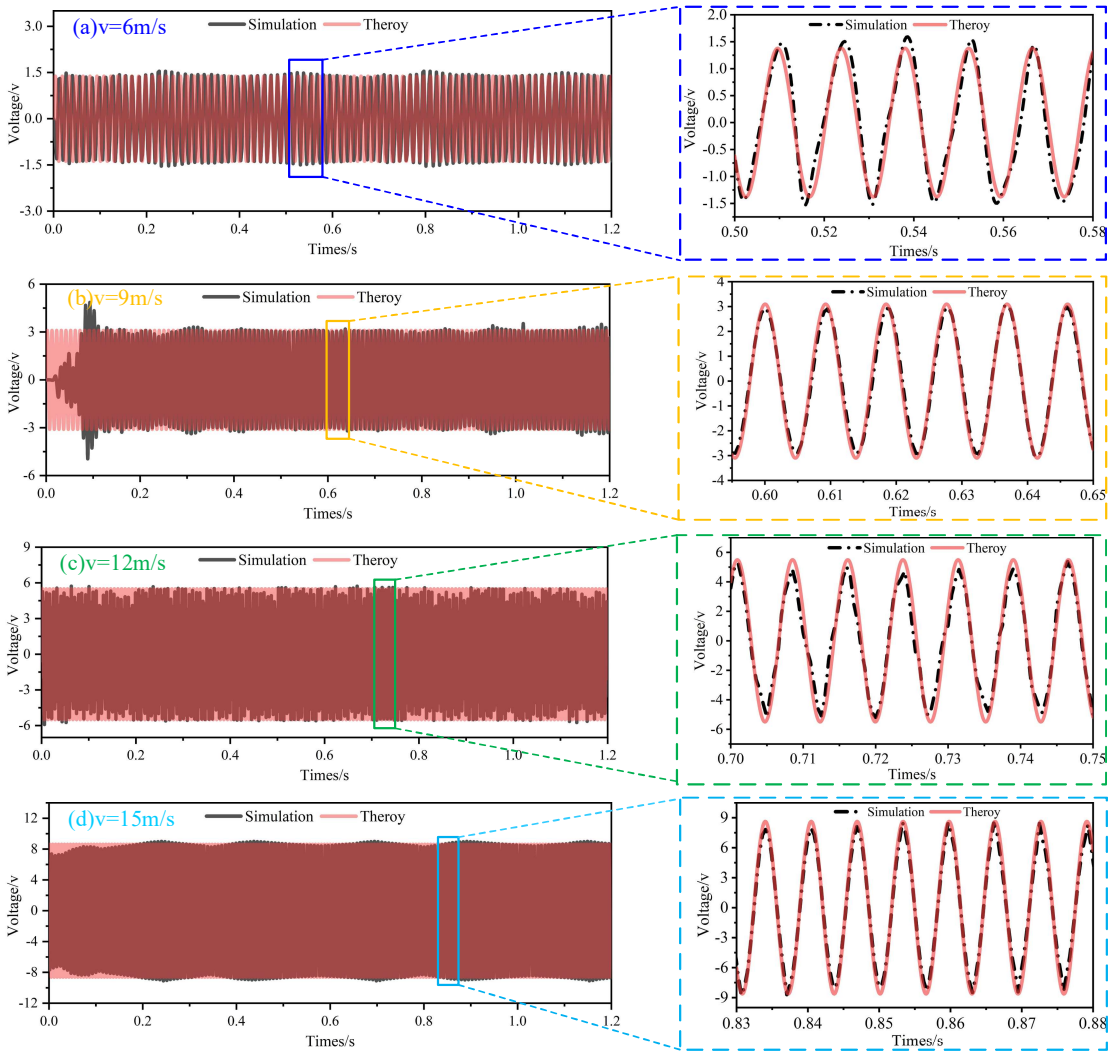

Fig.15 The comparison of output voltages between the simulation and theoretical values with the full-size the fluid-solid-electric physical model

In a cycle of the wave forward motion, the air outflows and inflows through the vent tunnel once following the up and down motion of OWC in the chamber. Correspondingly, the air velocity shows slight asymmetries during this process as shown in Fig.6. The time instantaneous air velocity at the orifice of the chamber corresponding to the free water surface is given by the theory in Eq.10 with the wave period T=2.5 s as shown in Fig.16(a). The results act as the input variable velocity in the interconnected VIV system analysis.

The detailed output information on the VIV-PEH is indicated in Fig.16(b-e) which shows the variation of the output voltage, and power related to the free end deflection of the cantilever beam. The time history curve comparison of the output open voltages is illustrated in Fig.16b and c with the simulation model and theoretical Eq.30 when the air flows past the bluff body with a diameter of 25 mm and the position parameter of d/d_D=4. As the wind speed gradually increases in the exhalation phase, the vortex shedding frequency gradually approaches the resonance frequency of the beam. The maximum output voltage is more than 10 V which agreed well with each other of simulational and theoretical values. The significance of the dynamic behavior is revealed by the deflection of the free end in Fig.16d. The power of the simulation model is slightly lower than the

theoretical results (seen in Fig.16e) because the output voltage decreases rapidly when the VIV exciting frequency departs from the intrinsic frequency of the PEH. On contrary, the theoretical results gradually decrease compared to Fig.16b and c. Another research consideration is the load resistance value for the maximum power output, which is generated for the resistance value of 11.8 kΩ as shown in Fig.16e.

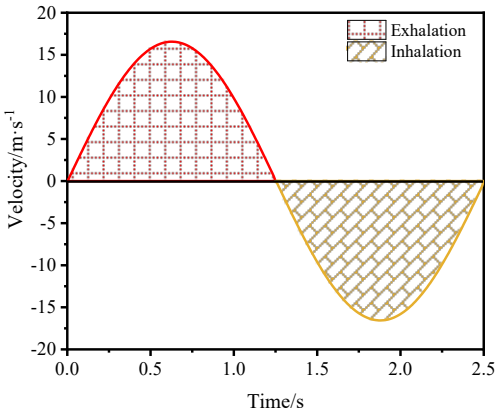

(a) Time instantaneous air velocity at the orifice of the chamber

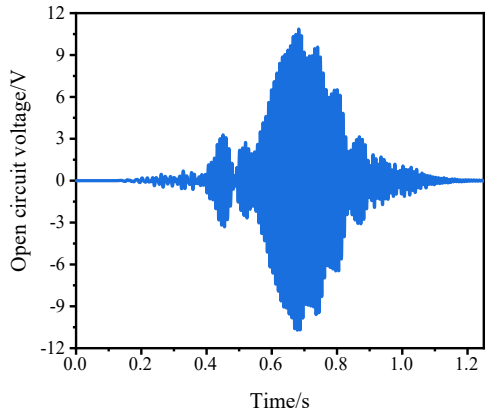

(b) Open voltage with simulation model

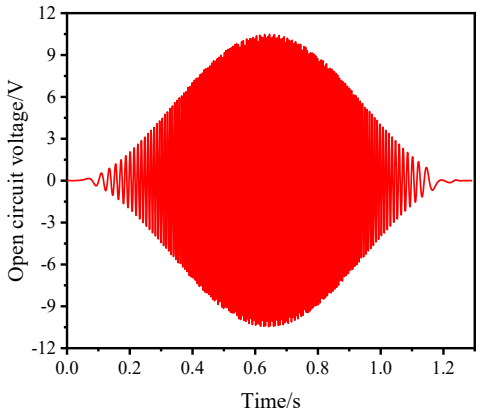

(c) Open voltage with the theoretical model

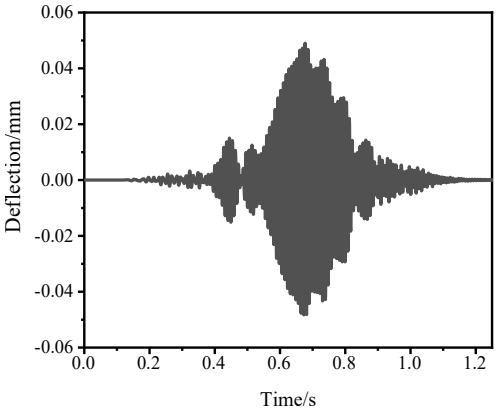

(d) Free end deflection of the piezoelectric cantilever beam

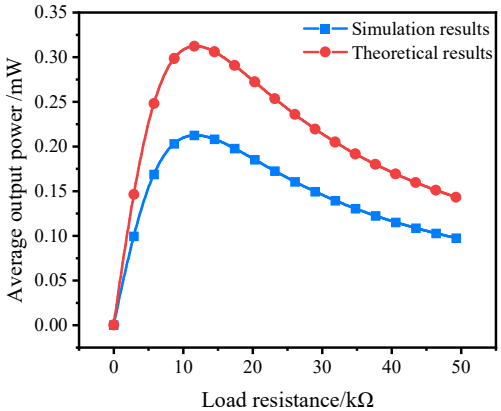

(e) Comparison of power between simulation and theoretical model

Fig.16 The output of voltage and power on the PEH

In the context of ocean wave energy harvesting, it is relevant to indicate the distribution of PEH in the vorticity and orientation of the vortex. The effective position in the wake of the VIV downstream of the bluff circular cylinder is adjusted by changing the relevant space between the bluff body and the beam to understand the imposed forces and wake pressure on the energy harvesting performance. The generated voltages are presented in Fig.17 for the different

attachment locations. The effective operating ranges for d/d_D are adjusted from 2, 3, 4, 5, to 6. At the location of d/d_D=2, it is close to the bluff body, the vorticity initially sheddings from the surface of the stationary cylinder and rolls forward as shown with the vorticity cloud in Fig.17a. The piezoelectric cantilever beam vibrates weakly with the minimum output voltage. The positive and negative vortices migrate to the upper and lower surfaces of the beam one after the other in the wake of the cylinder when the space expands to d/d_D=4. The interface performance was measured and compared to analytical and ANSYS results from Derakhshandeh's model[71]. The vorticity rolls forward with the momentum of an avalanche which forces the beam vibration violently in a transverse direction, generating the maximum electric power from the PEH. With the increase of d/d_D ratio, the intensity of the vortex reduces because it dissipates gradually due to the fluid viscosity. The output voltages in the time histories synchronously vary with the intensity of the vortex in Fig.17. Hence, the enclosure effect with the validated models has successfully demonstrated the benefits of location position VIV-PEH in the vent tunnel of the OWC chamber for the accuracy of the device as shown in Fig.17f.

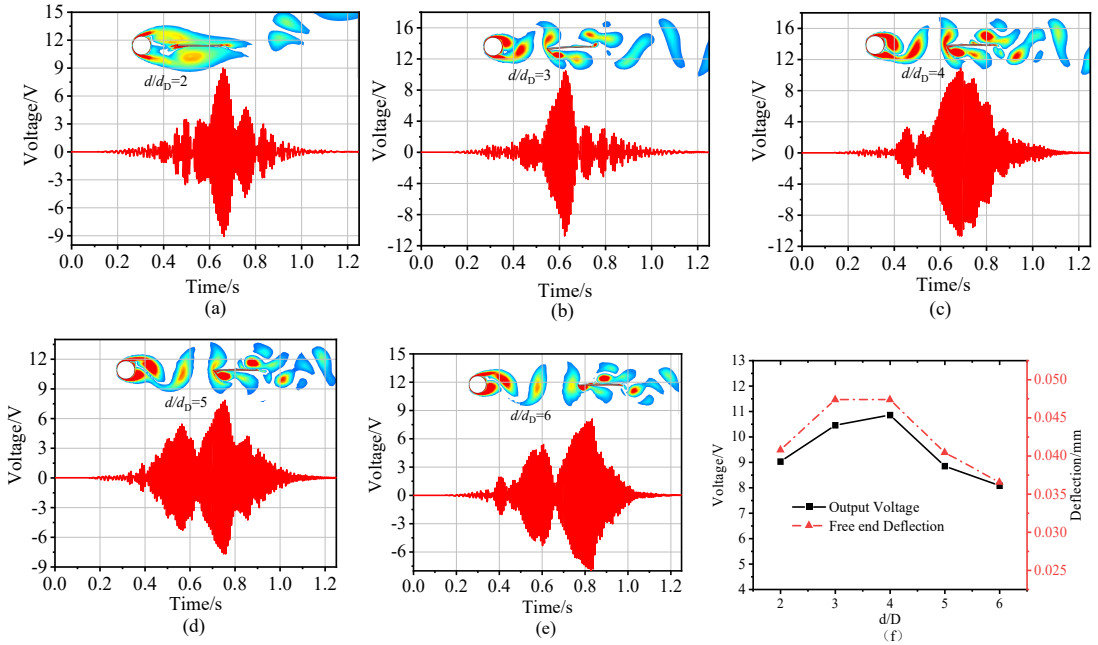

Fig.17 The effect position of PEH on voltage in the wakes

Moreover, to improve the piezoelectric energy harvesting power, the output electrical power is conducted versus the load resistance in the various instantaneous wind speeds. A series of computational analyses in the energy conversion structure and wind condition is investigated to explore the optimal load resistance as shown in Fig.18. The maximum output voltages of the VIV-PEHs increase with the increased load resistance. In the same terms, the powers increase firstly and then decrease which conforms to battery supply characteristics. At a wind velocity of 16.4 m/s and the location position ratio of d/d_D=4 the optimum performance is reached. The maximum output power is 3.55 mW with a load resistance of 8.1 kΩ. In summary, it can be concluded that the output electric power depends on the primary structure and the load resistance.

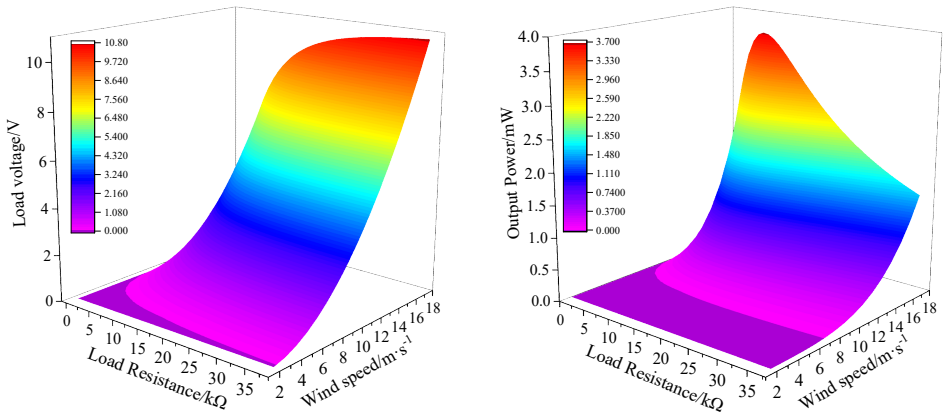

Fig.18 Summarized output voltages and power versus the load resistance and wind speed

5 Experiment and theoretical model verification

The hydrodynamic performance of the OWC chamber for primary wave extraction is experimentally measured in a wave-making flume at the Laboratory of Ocean Renewable Energy, Ocean University of China as shown in Fig19. The experiment schematic diagram is demonstrated in Fig.19a.The flume parameters of length, width, and water depth are 25 m, 1 m, and 0.6 m. An OWC chamber with a square horizontal cross-section is installed at a distance of 6 wavelengths from the push-plate wave-maker where the wave is regular and the reflected waves have been eliminated to reduce influences on the model as much as possible. The OWC surface goes up and down with the crests and troughs of the incident waves as shown in Fig.19b and c.

The system structure parameters of the OWC are given in Fig.19a which is built up with Acrylic board material and the transparent wall of the flume and OWC chamber helps easy to visualize and record the wave height in real-time as shown in Fig.19d. All of the examined results information is transformed into a digital signal for recording by a computer.

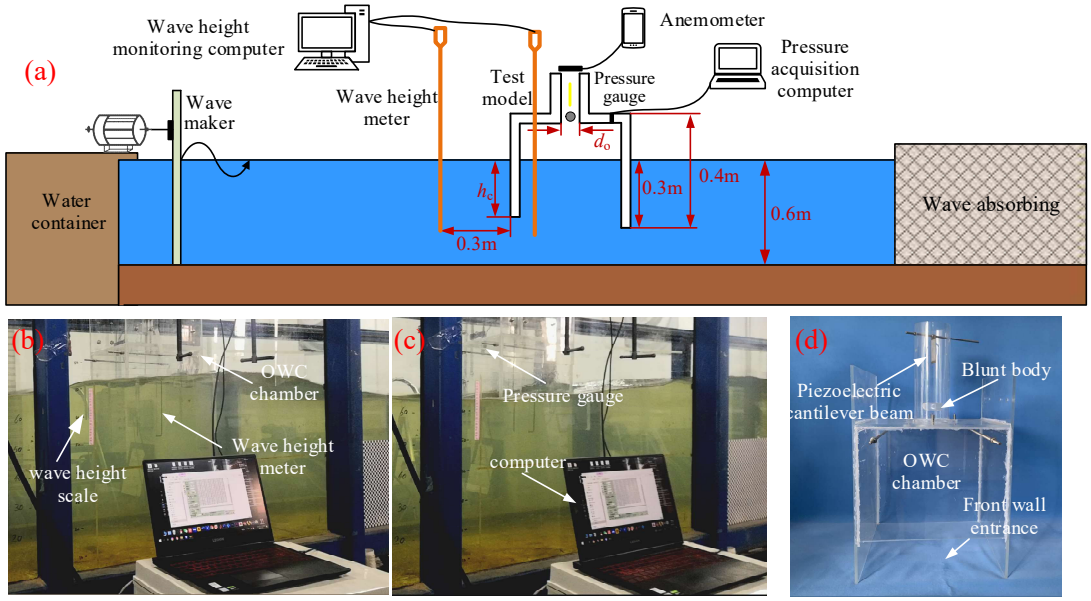

Fig.19 Wave flume and the OWC air chamber experiment

The time series of the water level inside and outside of the chamber is measured with the wave level meter for wave period T=1.5 s and the incident wave amplitude of 0.06 m, that is the outside wave height as shown in Fig.20a. As expected, the trends are in agreement with the

simulation results presented earlier in Fig.7a. Inside the chamber, water oscillates vertically with a lower amplitude than the outside surface. The damping force by air converts the potential energy of water into increasing aerodynamics pressure. The geometry optimization simulation for the models has been previously achieved in section 4 as shown in Fig.10. Accordingly, the objective of the carried-out experiments is to verify the influence of the submerged wall draft depth on airflow performance. As stated before, two variables h_c, d_c are monitored and the measured results are shown in Fig.20b. Correspondingly, the performance parameters of the air with experimental and theoretical models (in Eq.9) are compared in Figs.20c and d for the following wave and chamber conditions: h=0.06 m, T=1.5 s, and orifice dc=0.05 m. In addition to the good agreement between the CFD simulation model and theoretical results in section 4, Fig.20c and d show the reasonable matching between theoretical and experimental time series results. Hereto, these theoretical, experimental and CFD models provide extensive information to evaluate the wave energy conversion feasibility of the floating body and predict the air performance in the OWC chamber.

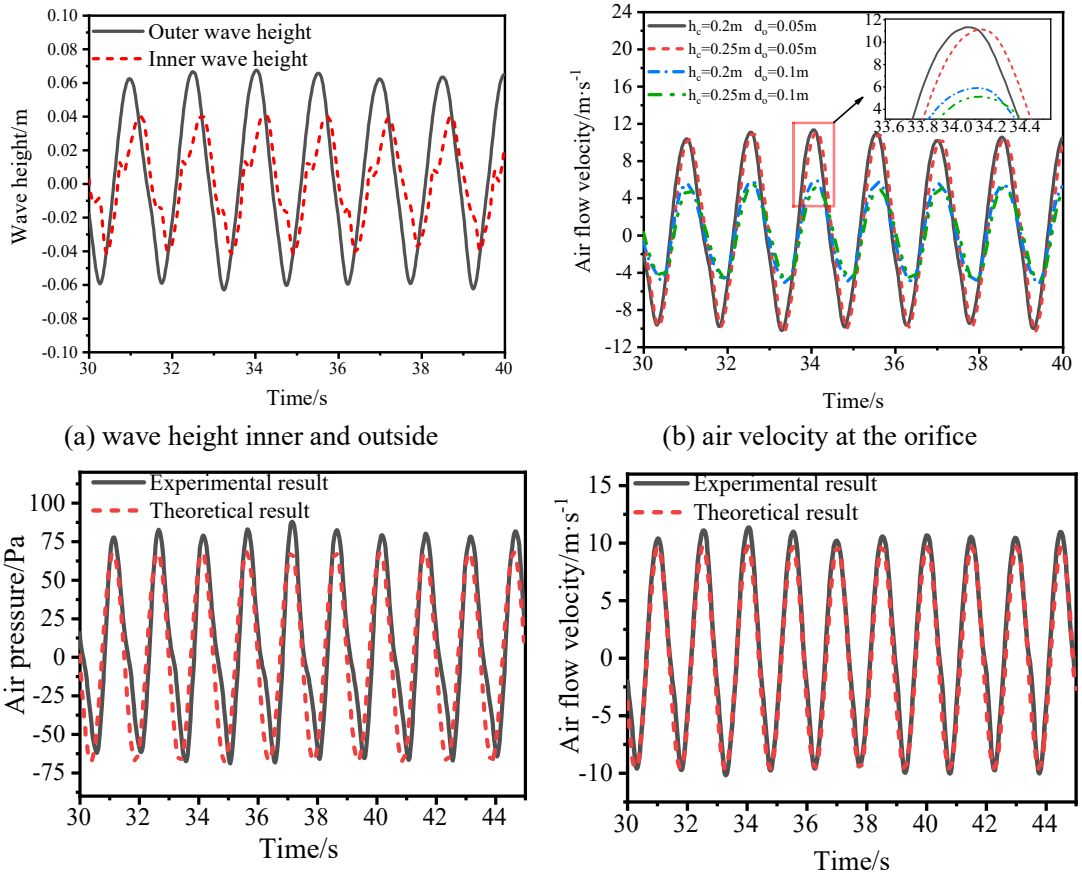

(a) wave height inner and outside

(b) air velocity at the orifice

(c) Air pressure at h_c=0.2 m

(d) Air velocity at h_c=0.2 m

Fig.20 The incident wave and the dynamic response of OWC and air in the chamber

The experimental platform is set up to evaluate the performance and verify the theoretical model of the proposed VIV-PEH energy harvester in the vent of the OWC chamber as shown in Fig.21.The prototype of the vortex-induced vibration piezoelectric power generation device is depicted in Fig.21a which is composed of an axial flow fan, bluff body, and piezoelectric cantilever beam. The bluff body is installed transverse to the upstream airflow to induce vortex vibration on the piezoelectric cantilever beam. The axial flow fan reproduces the airflow from the orifice of the OWC air chamber which flows past the wind tunnel instead of the vent tunnel. The wind speed variation can be controlled from 0 to 15 m/s with the variable frequency motor.

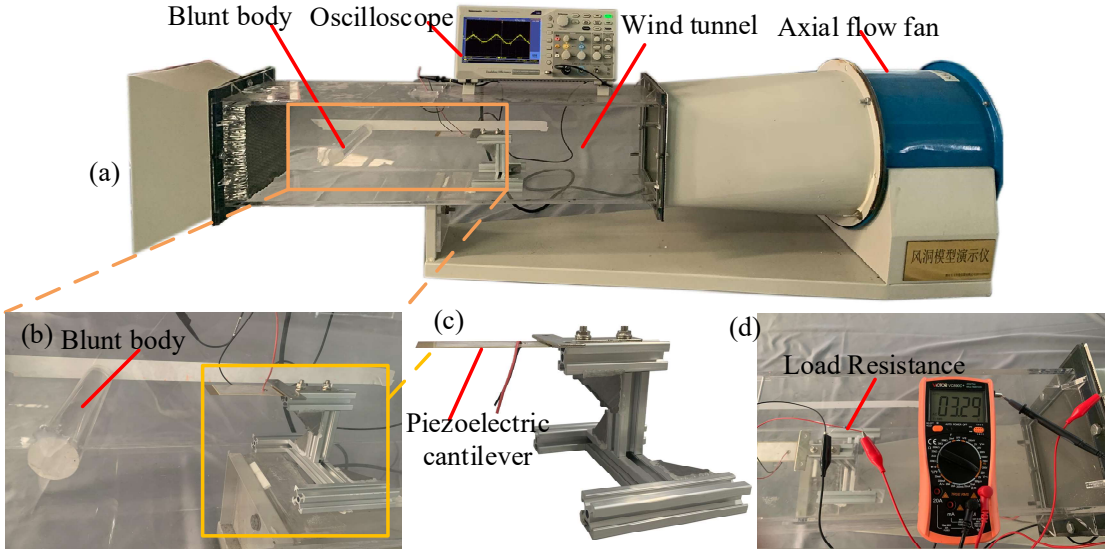

Fig.21 VIV-PEH experimental prototype

The piezoelectric cantilever beam is fixed in the wake of the bluff body as shown in Fig.21b. The output open circuit voltage of the piezoelectric layer was measured and recorded in real-time by a digital storage oscilloscope. The predicted theoretical values using Eq.30 and experimental output open circuit voltages with the induced vortex vibration wind velocity of 6 m/s, 9 m/s, 12 m/s, and 15 m/s are illustrated in Fig.22a and b, respectively. The theoretical and measured peak voltage reaches 8.62 V and 8.47 V, which are generated at a wind speed of 15 m/s. The results comparison indicates that the theoretical model provides a relatively accurate prediction for the induced voltages in the vortex wake region. In addition, to maximize the energy capture from this vibration source, the vortex shedding frequency coincides approximately with the natural frequency of the cantilever beam. The piezoelectric energy harvesting system extracts energy from the airflow or the ocean wave energy in resonance. More specifically, to investigate the application prospect of this novel power device for enhanced energy harvesting, the load resistance is set at 10 kΩ to predict the power harvesting capability. The output voltage and power are measured at preset various wind speeds as shown in Fig.23a. Results from these tests show that the output electric energy with certain resistor values rises significantly as the wind speed increases. For instance, when the wind speeds vary from 6 to 14 m/s, the voltage rises from 0.9 to 5.28 V, and the power moves from 0.316 mW to 1.4 mW. Additionally, the responses of voltage and power depend on the load resistance by the physical model from the experiment and theoretical simulation (Eq.31 and 32) are compared in Fig.23a and b. Hence, the derived model is validated for piezoelectric energy harvesting with a vortex-induced vibration.

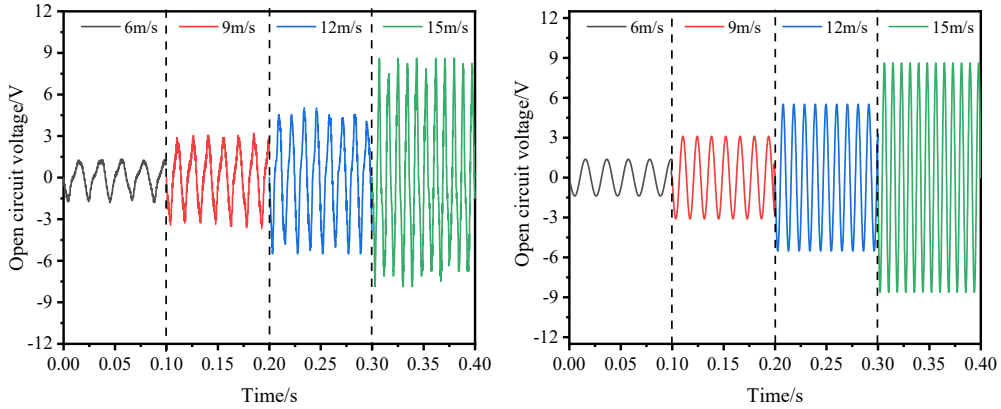

(a) Experiment with the physical model (b) Voltage with the theory model

Fig.22 Time history of the output open circuit voltage of VIV-PEH

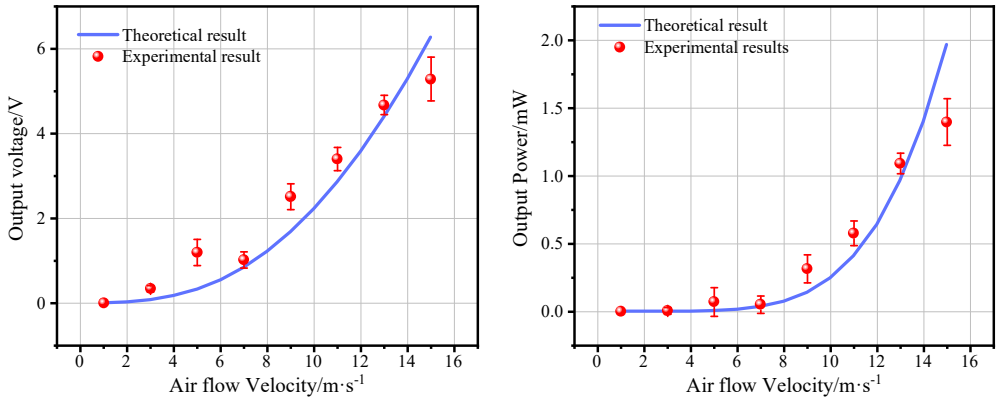

(a) output voltage (b) output power.

Fig.23 Comparison of experimental and theoretical results related to wind velocity on the load resistance of 10 KΩ

Furthermore, the correlation between measured and predicted power and output voltage varies with a range of load resistances at the wind speeds of 9 m/s, 12 m/s, and 14 m/s as shown in Fig.24. In the vent tunnel, the output power is maximized at the resistor with half of the open circuit voltage which agrees with the commonly accepted batteries power rule, that is, the voltages increase continuously and then tend to level off over a certain range of load resistances. The maximum power is achieved by the device at the optimum load resistance value of 13 kΩ when the wind speed is 15 m/s. The variation of output voltage and power generated from the harvester at three different wind speeds are matching well with the theoretical model for the considered optimum resistance value.

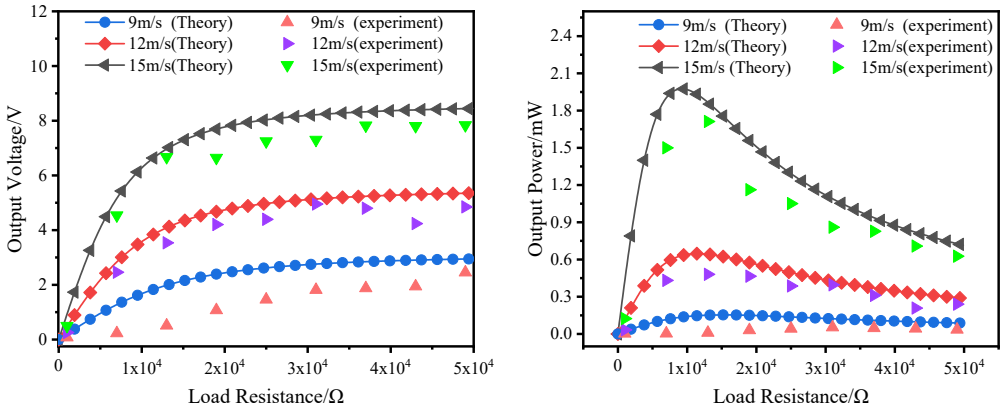

Fig.24 Output power with respect to the load resistance.

When the buoy floats at the ocean surface, it is noted that the water column oscillates in the chamber following the ocean wave motion. Consequently, the wind speeds vary with the exhalation and inhalation phases. With the validated theoretical model, the output electric power responses of the airflow wind speeds from the orifice are simulated to match the optimal load resistance as shown in Fig.25. The derived theory indicates that the piezoelectric energy harvesting system is insensitive to wind speed in the vent tunnel and the load resistance. This fact can be explained that the electromechanical coupling and the equivalent internal resistance of the piezoelectric generator change with the frequencies of the vortex-induced vibration downstream of the bluff body according to the wind speeds[72, 73].

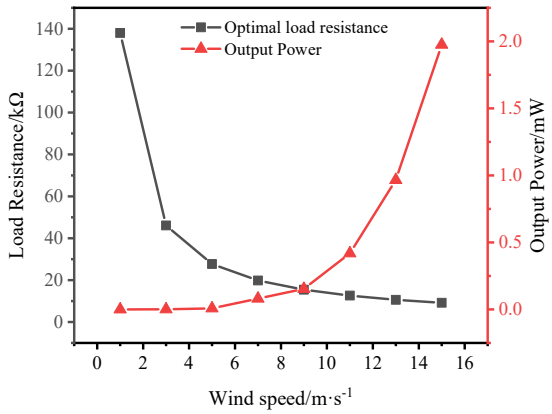

Fig.25 Power with wind speed and optimal load resistance

The power consumption requirements of sensors decreased tremendously to the milliwatts and even microwatts range with micro-electromechanical technology[74, 75]. The performance of the energy harvester is highly dependent on the ocean wave state, the operation conditions, dimensions of the air chamber and PEH, and piezoelectric materials employed that should be comprehensively evaluated according to the needs of the sensor's power. To compare the performance and the output power with the previous research literature, table 2 surveyed the typical micro energy harvester for the Up-converting frequency of the excitation source. Generally, the power generation performance and reliability of the Wave-VIVPEH can be designed according to the volume and space of the buoy. The output power of the Wave-VIVPEH could be improved as follows: it could work in a wind speed range of 10-20 $m \cdot s^{-1}$ in the vent tunnel of the air chamber. Furthermore, the scaling chamber could enlarge and extract more ocean wave energy to excite the piezoelectric vibrator and thus it can be operated in violent dynamic environments.

Table 2 Typical Up-converting frequency piezoelectric energy harvesters

Ref.	Technique	Piezoelectric Material	PEH dimensions (mm^3)	Excitation (Hz)	Frequency range(Hz)	Voltage(V)	Power
This work	Vortex upscaling	PZT	60×30×0.5	0~1	172	10.46	3.26 mW
Han Yu[76]	Rotating Seesaw Technology	PZT	20×30×0.3	2.94 ms^{-2}	19.18	49.15	4.03 mW
Ge Shi[77]	Magnetic coupling is driven by a rotating ball	PZT-5H	Device size: 280×280×60	0~1.4	5.5	17.2	6.32 mW

Lin-Chuan Zhao[78]	Dynamically synergistic regulation mechanism	PZT	37×30×0.3	Rotation speed between 0~1000r/min	17	122.1	1.6 mW
Yipeng Wu[79]	Internal resonance mechanism	PZT	-	1~5	12.27	20V	2 mW
Yan Wang[80]	flexible seaweed-like triboelectric	FEP PET PTFE	40×80×3	0.25~1.25	1.25	120.6	79.023 μW
Shao-En Chen[81]	Geared-Linkage Conversion Mechanism	PZT	78×25×0.158	1.17	6.44	2.8	1.37 μW
Miah Abdul Halim[82]	Transverse mechanical impact	PZT	40×6×0.5	5.2	818	12.53	93 μW
Meng Li[83]	Novel X-structured	MFC	100×18×0.3	2~4	12	25	109.08 μW
Seop Hwang[84]	Sway movement	PZT	38×19×0.2	0.5~1	31	21.1	68.9 μW

6. Conclusion

A vortex-induced frequency-up conversion for piezoelectric vibration generation is proposed to harvest ocean wave energy for the intelligent buoy. The ingenious system combines the advantages of the OWC wave capture device and piezoelectric coupling electro-mechanical transformation. When the chamber is contracted and inflated with the piston-like motion of the OWC, it exhales or inhales air through the vent tunnel. The bluff body is fixed inside the vent tunnel to convert the low-frequency and high-speed airflow into high-frequency eddy flow, which triggers the piezoelectric cantilever energy converter vibration. In the present analysis, the Wave-VIVPEH is investigated by theoretical, numerical and experimental methods. The water column oscillating in the chamber of the wave-making flume and the vortex-induced piezoelectric cantilever beam vibration in the wind tunnel are carried out respectively to experimentally validate the theoretical model. Furthermore, the theoretical and experimental responses agree well with the simulational results. The output voltage and power are compared with those found results, which verified the accuracy of the mathematical model. The maximum wind speed of 17.96 m/s and the pressure of 382.55 Pa in the OWC chamber were observed. A Wave-VIVPEH is constructed with the response of airflow from the ocean conditions. The output power characteristics of the piezoelectric energy harvester are analyzed for the distance of the vortex wake between the piezoelectric cantilever beam and the bluff body. With the bluff body diameter of 25 mm and distance of d/d_D=4, the theoretical results on the maximum peak voltage and output power are 10.46 V, 3.26mW agree with the simulation optimized values of the maximum peak voltage of 10.85V and the output power of 3.55 mW. When the wind speed is 15 m/s, the theoretical voltage of 8.62 V approaches the experimental result of 8.47 V. The Wave-VIVPEH technology is easily applied to more complex intelligent buoys or a multi-physics coupling energy conversion field,

furthermore, its application in the field of piezoelectric energy harvesting and VIV vibration is still in its infancy. Therefore, it is worth investing more research efforts to improve Wave-VIVPEH in engineering which promises the application of low-frequency wave energy harvesting and the possible implementation of self-power electronics on the intelligent buoy.

CRediT authorship contribution statement

X. Du: Conceptualization, Supervision, Writing – review & editing, Methodology. Y. Wang: Theory, Simulation, Experiment, Data analysis, Investigation, Writing original draft. H. Chen: Data analysis, Investigation. C. Li: Data curation. Y. Han: Formal analysis. D. Yurchenko: Writing and review & editing. J. Wang: Supervision, Review. H. Yu: Supervision, Writing – review & editing.

Declaration of interests

The authors declare that they have no known competing financial interests or personal relationships that could have appeared to influence the work reported in this paper.

Acknowledgment

This research was supported by the Natural Science Foundation of Shandong Province (ZR2021ME111). The authors gratefully acknowledge professor Tongshun Yu and his research group's support of the wave-making flume measured experiment at the Laboratory of Ocean Renewable Energy, Ocean University of China.

Appendix.A Detailed Solution Methodology on the velocity potential

The velocity potential is solved with Green's function with the finite depth of seawater which is represented as the combination of the singular and regular parts as follows:

$$G(P,t,Q,\tau)=\frac{\delta(t)}{r}+\frac{\delta(t)}{r_1}-2\delta(t)\int_0^\infty e^{-kh}\frac{\cosh(z+h)}{\cosh kh}\cosh(z+h)B_0(kR)\mathrm{d}k$$
$$+2\int_0^\infty\sqrt{gk}\frac{\cosh k(z+h)}{\cosh^2 kh\sqrt{\tanh kh}}\mathrm{d}k\times\int_0^t\sin[(t-\tau)\sqrt{gk\tanh kh}]\delta(\tau)\cosh(z+h)B_0(kR)\mathrm{d}\tau \tag{A.1}$$

where $\delta(t)$ is the impulse source; B_0 is the Bessel function of order zero; r is the distance between the domain point and the source point, and r_1 is the mirror distance to the seawater floor from the domain point to the source point; R is the horizontal distance from the domain point to the source point.

$$\left.\begin{aligned}R&=\sqrt{(x-x_0)^2+(y-y_0)^2}\\ r_0&=\sqrt{(x-x_0)^2+(y-y_0)^2+(z-z_0)^2}\\ r_1&=\sqrt{(x-x_0)^2+(y-y_0)^2+(2h+z+z_0)}\end{aligned}\right\} \tag{A.2}$$

Assuming the air chamber floats at the surface with the limited depth of the seawater, Green's function complies with the condition of a free water surface. The pulse source $\delta(t\text{-}\tau)$ at time τ will influence the flow field at time t that only relates to the time difference $(t\text{-}\tau)$. Assuming the pulse source $\delta(t)=1$, the Green's function is expressed as:

$$G(x,y,z,t)=\frac{1}{r}+\frac{1}{r_1}-2\int_0^{\infty}e^{-kh}\frac{\cosh k(z_0+h)}{\cosh kh}\cosh k(z+h)B_0(kR)\mathrm{d}k$$
$$+2\int_0^{\infty}\frac{\cosh k(z+h)}{\cosh kh\sinh kh}\cosh k(z_0+h)\times\{1\text{-}\cos[(t\text{-}\tau)\sqrt{gk\tanh kh}]\}B_0(kR)\mathrm{d}k \tag{A.3}$$

Green's function satisfies the Laplace equation, that is $\nabla^2 G=-\delta(t-\tau)\delta(x-x_0)$.

In the inner region, $t\geq\tau$, the initial boundary condition is given as follows:

At the free surface of the OWC: $G_t+\mathrm{g}G_\tau=0$, $t>\tau$.

On the ocean floor: $\frac{\partial G}{\partial n}=0$, z=-h, $t\geq\tau$

At infinity away from the air chamber $\lim_{R\to\infty}\nabla G=0$, $t\geq\tau$

Green's function is divided into two components of the instantaneous item G^{i} and the memory item G^{f}.

$$G(x,t,x_0,\tau)=\delta(t-\tau)G^{\mathrm{i}}(x,x_0)+G^{\mathrm{f}}(x,t;x_0,\tau) \tag{A.4}$$

$$G^{\mathrm{i}}(x,x_0)=\frac{1}{r}+\frac{1}{r_1}-2\int_0^{\infty}\frac{e^{-kh}}{\cosh kh}\psi(z,z_0,R)\mathrm{d}k \tag{A.5}$$

$$G^{\mathrm{f}}(x,t;x_0,\tau)=\int_0^{\infty}\frac{1}{\cosh kh\sinh kh}\left[1-\cos(t-\tau)\sqrt{gk\tanh kh}\right]\psi(z,z_0,R)\mathrm{d}k \tag{A.6}$$

where $\psi(z,z_0,R)=\cosh\left[k(z_0+h)\right]\cosh\left[k(z+h)\right]B_0kR$

The function in Eq.(A.1) contains the sinusoidal and Bessel function, therefore, the integrals will converge slowly. The calculation is more complicated with high-frequency oscillation items and the slow convergence of the integration process. Wehausen and Laiton solved the Green function with a 3D pulsation source based on the boundary condition[85] Furthermore, the dimensionless transformation of g and h will improve the calculation accuracy[86].

$$X=\frac{R}{\mathrm{h}},Y=-\frac{z_0}{\mathrm{h}},Z=-\frac{z}{\mathrm{h}},T=(t\text{-}\tau)\sqrt{\frac{g}{\mathrm{h}}}$$

Thus, the green function is rewritten as follows. The instantaneous item G^0 and the memory item G^{f} in Eq.(A.4) are described by G_0 and G_1 respectively in Eq.(A.7).

$$G=h^{-1}[G_0(X,Y-Z)+G_0(X,2-Y-Z)]$$
$$-\mathrm{g}^{\frac{1}{2}}h^{\frac{3}{2}}[G_1(X,Y-Z,T)+G_1(X,2-Y-Z,T)] \tag{A.7}$$

In accordance with dimensionless transformation, further, the instantaneous item G^{i} and memory item G^{f} in Green's function is rewritten correspondingly.

$$G_0(X,V)=\frac{1}{\sqrt{X^2+V^2}}-\int_0^{\infty}\mathrm{e}^{-u}\frac{\sinh u}{\cosh u}\cosh(uV)B_0(uX)\mathrm{d}u \tag{A.8}$$

$$G_1(X,V,T)=\int_0^{\infty}\frac{\sqrt{k\tan k}}{\cosh k\sinh k}\sin(T\sqrt{k\tanh k})\cosh(kV)B_0(kX)\mathrm{d}k \tag{A.9}$$

where u=kh is the integral variable, and V is a code symbolic variable to simplify the equation.

Firstly, the instantaneous item G^0 is solved. The Green function is calculated by the multi-dimensional Chebyshev polynomial approximation method[86]. Furthermore, to calculate

G^0 quickly, it is solved by subsection according to the variate X. In the far domain of the wave field, that is $X>1$, G_0 is described by the Fourier series.

$$G_0(X,V)=2\sum_{m=0}^{\infty}\cos\left[(m+\frac{1}{2})\pi V\right]K_0\left[(m+\frac{1}{2})\pi X\right] \tag{A.10}$$

where K_0 is amended Hankel function[87].

In the near domain of the wave field, that is $0\leqslant X\leqslant 1$ and $0\leqslant V\leqslant 2$, the calculation value will approach $G_0(X, V)$ by the Chebyshev polynomial approximation method.

$$G_0(X,V)=\frac{1}{\sqrt{X^2+V^2}}-\frac{1}{\sqrt{X^2+(V+2)^2}}-\frac{1}{\sqrt{X^2+(V-2)^2}}-\sum_{m\cdot n}a_{mn}x^{2m}v^{2n}+1-\ln 2 \tag{A.11}$$

where a_{mn} is the interpolation coefficient of fast calculation determined for the Green function within the various parameter ranges.

$$a_{0n}=\frac{1}{(n+1)(n+1)!}$$

$$a_{mn}=(-1)^m\frac{(n+2)(n+4)\cdots(n+2mn)}{\left[(n+1)(n+3)\cdots(n+2m+1)\right](n+2m+1)!}$$

$$m=1,2,3\ldots;n=0,1,2,3\ldots$$

In addition, if $0\leqslant X\leqslant 1$, the partial derivatives of X and V in the multinomial equation $G_0(X, V)$ are given separately.

$$\frac{\partial G_0}{\partial X}=-\frac{X}{(X^2+V^2)^{\frac{3}{2}}}+\frac{X}{[X^2+(V+2)^2]^{\frac{3}{2}}}+\frac{X}{\left[X^2+(V-2)^2\right]^{\frac{3}{2}}}+2\sum_{m,n}ma_{mn}X^{2m-1}V^{2n} \tag{A.12}$$

$$\frac{\partial G_0}{\partial V}=-\frac{V}{(X^2+V^2)^{\frac{3}{2}}}+\frac{V+2}{\left[X^2+(V+2)^2\right]^{\frac{3}{2}}}+\frac{V-2}{\left[X^2+(V-2)^{\frac{3}{2}}\right]^{\frac{3}{2}}}+2\sum_{m,n}na_{mn}X^{2m}V^{2n-1} \tag{A.13}$$

If $X>1$ the partial derivatives are given.

$$\frac{\partial G_0}{\partial X}=-2\sum_{m=0}^{\infty}\left(m+\frac{1}{2}\right)\pi\cos\left[\left(m+\frac{1}{2}\right)\pi V\bullet K_1[\left(m+\frac{1}{2}\right)\pi X]\right] \tag{A.14}$$

$$\frac{\partial G_0}{\partial V}=-2\sum_{m=0}^{\infty}\left(m+\frac{1}{2}\right)\pi\sin\left[\left(m+\frac{1}{2}\right)\pi V\bullet K_0[\left(m+\frac{1}{2}\right)\pi X]\right] \tag{A.15}$$

where K_1 is the first order of the modified Hankel function.

The dimensionless coefficients are substituted into the above equations, respectively, where the instantaneous item G^{i} and the partial derivatives on the variable are derived.

$$G^{\mathrm{i}}=h^{-1}[G_0(X,Y-Z)+G_0(X,2-Y-Z)] \tag{A.16}$$

$$\begin{aligned}G_x^{\mathrm{i}}&=h^{-1}[G_{0X}(X,Y-Z)+G_{0X}(X,2-Y-Z)]\frac{\partial X}{\partial R}\frac{\partial R}{\partial x}\\&=h^{-1}[G_{0X}(X,Y-Z)+G_{0X}(X,2-Y-Z)]\frac{1}{h}\frac{x-x_0}{R}\\&=\frac{x-x_0}{Rh^2}[G_{0X}(X,Y-Z)+G_{0X}(X,2-Y-Z)]\end{aligned} \tag{A.17}$$

$$G_y^{\mathrm{i}} = h^{-1}[G_{0X}(X,Y-Z)+G_{0X}(X,2-Y-Z)]\frac{\partial X}{\partial R}\frac{\partial R}{\partial y}$$
$$= h^{-1}[G_{0X}(X,Y-Z)+G_{0X}(X,2-Y-Z)]\frac{1}{h}\frac{y-y_0}{R} \quad (A.18)$$
$$= \frac{y-y_0}{Rh^2}[G_{0X}(X,Y-Z)+G_{0X}(X,2-Y-Z)]$$

$$G_z^{\mathrm{i}} = h^{-1}[G_{0V}(X,Y-Z)+G_{0V}(X,2-Y-Z)]\frac{\partial V}{\partial Z}\frac{\partial Z}{\partial z}$$
$$= h^{-1}[G_{0V}(X,Y-Z)+G_{0V}(X,2-Y-Z)](-1)(-\frac{1}{h}) \quad (A.19)$$
$$= \frac{1}{h^2}[G_{0V}(X,Y-Z)+G_{0V}(X,2-Y-Z)]$$

Secondly, according to the dimensionless substitution, the memory item G^{f} and G_1 are solved as follows.

$$G_1\left(X,V,T\right) = \int_0^\infty \frac{\sqrt{k\tanh k}}{\cosh k \sinh k}\sin\left(T\sqrt{k\tanh k}\right)\cosh\left(kV\right)\mathrm{B}_0\left(kX\right)\mathrm{dk} \quad (A.20)$$

Under the hyperbolic function approach,

$$\cosh kV = \frac{\mathrm{e}^{kV}+\mathrm{e}^{-kV}}{2},\quad \cosh k = \frac{\mathrm{e}^{k}+\mathrm{e}^{-k}}{2},\quad \sinh k = \frac{\mathrm{e}^{k}-\mathrm{e}^{-k}}{2}$$

Here, it can be derived following function further.

$$\frac{\cosh kV}{\cosh k \sinh k} = \frac{2\left(\mathrm{e}^{kV}+\mathrm{e}^{-kV}\right)}{\mathrm{e}^{2k}-\mathrm{e}^{-2k}}\times\frac{\mathrm{e}^{-2k}}{\mathrm{e}^{-2k}} = \frac{2\left(\mathrm{e}^{k(V-2)}+\mathrm{e}^{-k(V+2)}\right)}{1-\mathrm{e}^{-4k}}$$

Hence, Eq.(A.20) is simplified as.

$$G_1\left(X,V,T\right) = 2\int_0^\infty \sqrt{k\tanh k}\sin\left(T\sqrt{k\tanh k}\right)\frac{\mathrm{e}^{k(V-2)}+\mathrm{e}^{-k(V+2)}}{1-\mathrm{e}^{-4k}}B_0\left(kX\right)dk \quad (A.21)$$

When the domain point closes gradually to the source point for the solution procedure of the Green function of $G_1(X, V, T)$, it may contain the singularities which oscillate fastly and hardly converge. Therefore, the oscillation item $G_{1\infty}$ should be separated as follows.

$$G_1(X,V,T) = G_{1\infty} + (G_1 - G_{1\infty}) \quad (A.22)$$

$$G_{1\infty} = \lim_{k\to\infty} G_1(X,V,T)$$
$$= \lim_{k\to\infty}\int_0^\infty \frac{\sqrt{k\tanh k}}{\cosh k \sinh k}\sin\left(T\sqrt{k\tanh k}\right)\cosh(kV)B_0\left(kX\right)dk \quad (A.23)$$

When $k\to\infty$, Eq.(A.23) can be simplified.

$$G_{1\infty} = 2\int_0^\infty \sqrt{k}\sin\left(T\sqrt{k}\right)\mathrm{e}^{k(V-2)}\,\mathrm{B}_0(kX)\mathrm{d}k \quad (A.24)$$

The corresponding subtraction in Eq.(A.22) is given.

$$G_1 - G_{1\infty} = 2\int_0^{\infty} \sqrt{k} B_0(kX) \left[\sqrt{\tanh k} \sin\left(T\sqrt{k\tanh k}\right) \frac{e^{k(V-2)} + e^{-k(V+2)}}{1-e^{-4k}} - \sin\left(T\sqrt{k}\right) e^{k(V-2)} \right] dk \quad (A.25)$$

According to the dimensionless space coordinates, the space and time derivatives of function $G_{1\infty}$ are described.

$$G_{1\infty}\big|_X = -2\int_0^{\infty} k^{3/2} \sin(T\sqrt{k}) e^{k(V-2)} B_1(kX) dk \quad (A.26)$$

$$G_{1\infty}\big|_V = 2\int_0^{\infty} k^{3/2} \sin(T\sqrt{k}) e^{k(V-2)} B_0(kX) dk \quad (A.27)$$

$$G_{1\infty}\big|_T = 2\int_0^{\infty} k \cos(T\sqrt{k}) e^{k(V-2)} B_0(kX) dk \quad (A.28)$$

Conveniently, $G_{1\infty}$ can be converted into spherical coordinates (r, θ). The angle θ is measured from the negative vertical axis[86]. In the spherical coordinates, the dimensionless physical parameters variables are replaced as follows:

$r = \sqrt{X^2 + (V-2)^2}$; V-2=-$r$cosθ; X=$r$sinθ; τ=T/$\sqrt{r}$,

Thus, $G_{1\infty}$ is rewritten as:

$$G_{1\infty} = r^{-\frac{3}{2}} \mathrm{Re}\{-2i\int_0^{\infty} \sqrt{k} \exp\left(i\tau\sqrt{k} - k\cos\theta\right) B_0(k\sin\theta) dk\} \quad (A.29)$$

Correspondingly, the derivatives $G_{1\infty}$ are redescribed in the spherical coordinates as follows.

$$G_{1\infty}\big|_X = -r^{-5/2} \mathrm{Re}\left\{-2i\int_0^{\infty} k^{3/2} \exp\left(i\tau\sqrt{k} - k\cos\theta\right) B_1(k\sin\theta) dk\right\} \quad (A.30)$$

$$G_{1\infty}\big|_V = -r^{-5/2} \mathrm{Re}\left\{-2i\int_0^{\infty} k^{3/2} \exp\left(i\tau\sqrt{k} - k\cos\theta\right) B_0(k\sin\theta) dk\right\} \quad (A.31)$$

$$G_{1\infty}\big|_T = -r^{-2} \mathrm{Re}\left\{2\int_0^{\infty} k \exp\left(i\tau\sqrt{k} - k\cos\theta\right) B_0(k\sin\theta) dk\right\} \quad (A.32)$$

where B_1 is the first order of the Bessel function.

Similarly, the derivatives $G_1 - G_{1\infty}$ are redescribed.

$$\left(G_1 - G_{1\infty}\right)\big|_X = -2\int_0^{\infty} k^{3/2} B_1(kX) \left[\sqrt{\tanh k} \sin\left(T\sqrt{k\tanh k}\right) \frac{e^{k(V-2)} + e^{-k(V+2)}}{1-e^{-4k}} - \sin\left(T\sqrt{k}\right) e^{k(V-2)} \right] dk \quad (A.33)$$

$$\left(G_1 - G_{1\infty}\right)\big|_V = 2\int_0^{\infty} k^{3/2} B_0(kX) \left[\sqrt{\tanh k} \sin\left(T\sqrt{k\tanh k}\right) \frac{e^{k(V-2)} - e^{-k(V+2)}}{1-e^{-4k}} - \sin\left(T\sqrt{k}\right) e^{k(V-2)} \right] dk \quad (A.34)$$

$$\left(G_1 - G_{1\infty}\right)\big|_T = 2\int_0^{\infty} k B_0(kX) \left[\sqrt{\tanh k} \cos\left(T\sqrt{k\tanh k}\right) \frac{e^{k(V-2)} - e^{-k(V+2)}}{1-e^{-4k}} - \cos\left(T\sqrt{k}\right) e^{k(V-2)} \right] dk \quad (A.35)$$

The dimensionless space coordinates variates are substituted into the above equations, hence, the memory item G^{f} and its derivatives in the limited depth of the seawater are given.

$$G^{\mathrm{f}} = -g^{\frac{1}{2}}h^{-\frac{3}{2}}[G_1(X,Y-Z,T)+G_1(X,2-Y-Z,T)] \tag{A.36}$$

$$\begin{aligned} G_x^{\mathrm{f}} &= -g^{\frac{1}{2}}h^{-\frac{3}{2}}[G_{1X}(X,Y-Z,T)+G_{1X}(X,2-Y-Z,T)]\frac{\partial X}{\partial R}\frac{\partial R}{\partial x} \\ &= -g^{\frac{1}{2}}h^{-\frac{3}{2}}[G_{1X}(X,Y-Z,T)+G_{1X}(X,2-Y-Z,T)]\frac{1}{h}\frac{x-x_0}{R} \\ &= \frac{(x-x_0)(-g^{\frac{1}{2}}h^{-\frac{5}{2}})}{R}[G_{1X}(X,Y-Z,T)+G_{1X}(X,2-Y-Z,T)] \end{aligned} \tag{A.37}$$

$$\begin{aligned} G_y^{\mathrm{f}} &= -g^{\frac{1}{2}}h^{-\frac{3}{2}}[G_{1X}(X,Y-Z,T)+G_{1X}(X,2-Y-Z,T)]\frac{\partial X}{\partial R}\frac{\partial R}{\partial y} \\ &= -g^{\frac{1}{2}}h^{-\frac{3}{2}}[G_{1X}(X,Y-Z,T)+G_{1X}(X,2-Y-Z,T)]\frac{1}{h}\frac{y-y_0}{R} \\ &= \frac{(y-y_0)(-g^{\frac{1}{2}}h^{-\frac{5}{2}})}{R}[G_{1X}(X,Y-Z,T)+G_{1X}(X,2-Y-Z,T)] \end{aligned} \tag{A.38}$$

$$\begin{aligned} G_z^{\mathrm{f}} &= -g^{\frac{1}{2}}h^{-\frac{3}{2}}[G_{1V}(X,Y-Z,T)+G_{1V}(X,2-Y-Z,T)]\frac{\partial V}{\partial Z}\frac{\partial Z}{\partial z} \\ &= -g^{\frac{1}{2}}h^{-\frac{3}{2}}[G_{1V}(X,Y-Z,T)+G_{1V}(X,2-Y-Z,T)]\times(-1)\times(-\frac{1}{h}) \\ &= -g^{\frac{1}{2}}h^{-\frac{5}{2}}[G_{1V}(X,Y-Z,T)+G_{1V}(X,2-Y-Z,T)] \end{aligned} \tag{A.39}$$

$$\begin{aligned} G_\tau^{\mathrm{f}} &= -g^{\frac{1}{2}}h^{-\frac{3}{2}}[G_{1T}(X,Y-Z,T)+G_{1T}(X,2-Y-Z,T)]\frac{\partial T}{\partial \tau} \\ &= -g^{\frac{1}{2}}h^{-\frac{3}{2}}[G_{1T}(X,Y-Z,T)+G_{1T}(X,2-Y-Z,T)]\times(-\sqrt{\frac{g}{h}}) \\ &= \frac{g}{h^2}[G_{1T}(X,Y-Z,T)+G_{1T}(X,2-Y-Z,T)] \end{aligned} \tag{A.40}$$

With the finite depth of water, the maximum wave group velocity is $\sqrt{gh}$. The most forward boundary of the wave group is $t\sqrt{gh}$ or X=T. Meanwhile, the waves in the chamber are restricted to the range of $X \le T$. The Bessel sine function in Eq.(A.24) will bring the integrand about high-speed oscillation. As a result, it is difficult to directly calculate with the general quadrature formula. Here, the gradual approach calculation method is adopted by Newman[87].

When X<<T, In the wave region of $X \le T$, the $G_1(X, V, T)$ function contains a steady item and an oscillating item. G_1 is expressed as:

$$G_1(X,V,T) = \mathrm{Re}\{g_0 + g_1 + g_2\} \tag{A.41}$$

$$g_0 = -2i\int_0^{i\frac{\pi}{4}} \frac{\omega}{\sinh 2k}\cosh kV\mathrm{e}^{i\omega T}\mathrm{B}_0(kX)\mathrm{d}k \tag{A.42}$$

$$g_{1,2} = -i\int_0^{i\frac{\pi}{4}} \frac{\omega}{\sinh 2k}\cosh kV\mathrm{e}^{i\omega T}\mathrm{H}_0^{(1,2)}(kX)\mathrm{d}k \tag{A.43}$$

$$\omega(k) = \sqrt{k\tanh k} \tag{A.44}$$

The g_0, g_1, and g_2 are solved with the asymptotic expansion method.

$$\begin{aligned} g_0 = {} & (T^2 - X^2)^{-\frac{1}{2}} + (\frac{5}{6} - \frac{1}{2}V^2)(2T^2 + X^2)(T^2 - X^2)^{-\frac{5}{2}} - \\ & \frac{1}{2}T^2(2T^2 + X^2)(T^2 - X^2)^{-\frac{7}{2}} + O(T^4(T^2 - X^2)^{-\frac{9}{2}}) \end{aligned} \tag{A.45}$$

$$\mathrm{Re}(g_1 + g_2) \cong 2\sqrt{\frac{\tanh k_0}{\left|\omega_0^{''}\right| XT}}\frac{\cosh k_0 V}{\sinh 2k_0}\sin(\omega_0 T - k_0 X) \tag{A.46}$$

where k_0 is the root of the transcendental equation $\omega_0 = \omega(k_0)$, $\omega^{'}(k) = X/T$, $\omega_0^{''} = \omega^{''}(k_0)$.

Likewise, when $X \approx T >> 1$ the function G_1 can be solved with the asymptotic expansion method.

$$G_1(X,V,T) \cong 2^{\frac{1}{3}}\pi T^{-\frac{2}{3}}[\mathrm{Ai}(-(\frac{1}{4}T)^{\frac{2}{3}}(1 - \frac{X^2}{T^2}))]^2 \tag{A.47}$$

where Ai () is the Airy function[88].

When X>>T, $k = \mathrm{i}\kappa, \Omega(\kappa) = -\mathrm{i}\omega(k) = \sqrt{\kappa\tan\kappa}$, κ_0 be the root of the transcendental equation $\Omega^{'}(\kappa) = X/T, \Omega^{'}(\kappa_0) = X/T, \Omega_0 = \Omega(\kappa_0), \Omega_0^{''} = \Omega^{''}(\kappa_0)$, hence, G_1 is expressed:

$$G_1(X,V,T) = \mathrm{Im}\int_0^{\infty} \frac{\omega}{\sinh 2k}\cosh kV(\mathrm{e}^{i\omega T} - \mathrm{e}^{-i\omega T})H_0^{(1)}(kX)\mathrm{d}k \tag{A.48}$$

where Im() is the imaginary part of the integral.

Furthermore, at the moving head of the wave (X>>T), $G_1(X, V, T)$ is an exponential function, And the variation trend is relatively gentle. The path integral is from 0 to $\mathrm{i}\kappa_0$ along the imaginary axis, and that parallels the real axis to $k = +\infty\mathrm{i}\kappa_0$, the saddle point $\mathrm{i}\kappa_0$. With the gradient descent method, G_1 and its derivative are expressed:

$$G_1(X,V,T) \cong \sqrt{\frac{\tan\kappa_0}{\Omega_0^{''}XT}}\frac{\cos\kappa_0 V}{\sin 2\kappa_0}\exp(\Omega_0 T - \kappa_0 X) \tag{A.49}$$

$$G_1(X,V,T)\big|_X \cong -\kappa_0\sqrt{\frac{\tan\kappa_0}{\Omega_0^{''}XT}}\frac{\cos\kappa_0 V}{\sin 2\kappa_0}\exp(\Omega_0 T - \kappa_0 X) \tag{A.50}$$

$$G_1(X,V,T)\big|_V \cong -\kappa_0\sqrt{\frac{\tan\kappa_0}{\Omega_0^{''}XT}}\frac{\sin\kappa_0 V}{\sin 2\kappa_0}\exp(\Omega_0 T - \kappa_0 X) \tag{A.51}$$

$$G_1(X,V,T)\big|_T \cong -\Omega_0\sqrt{\frac{\tan\kappa_0}{\Omega_0'' XT}}\frac{\cos\kappa_0 V}{\sin 2\kappa_0}\exp(\Omega_0 T-\kappa_0 X) \tag{A.52}$$

When $X<T$, the G_1 is an infinite interval integral function, and to accelerate the integration convergence, $G_1(X, V, T)$ is solved with a factorization method based on Eq.(A.22). When the field point is close to the source point, the singularity problem will be involved as:

$$G_1^{\infty} = G_{10}^{\infty} + G_{11}^{\infty} \tag{A.53}$$

$$G_{10}^{\infty} = 2\int_0^{\infty}\sin(\sqrt{k}T)\mathrm{e}^{k(V-2)}\mathrm{d}k \tag{A.54}$$

$$G_{11}^{\infty} = 2\int_0^{\infty}\sin(\sqrt{k}T)\mathrm{e}^{k(-V-2)}\mathrm{d}k \tag{A.55}$$

G_1-$G_{1\infty}$ polynomial approximate calculation of any continuous function f(x)(-1≤x≤1) can be calculated by Chebyshev polynomial expansion[89].

$$f(X)\approx\sum_{m=0}^{N}c_m T_m(X) \tag{A.56}$$

$$c_m = \frac{\varepsilon_m}{N}\sum_{n=0}^{N}{}''f(X_n)T_m(X_n) \tag{A.57}$$

When m>2, $\varepsilon_0=1$, $\varepsilon_m=2$, the double prime on the summation sign means that the first item and the last item are multiplied by 1/2. And the number of truncated items n is selected to make the Chebyshev series sum to any precision. Use relational expression

$$T_n(X)=\frac{1}{2}n\sum_{m=0}^{n/2}(-1)^m\frac{(n-m-1)!}{m!(n-m)!}(2X)^{n-2m} \tag{A.58}$$

According to the approximate properties of Chebyshev polynomials, the item G_1-$G_{1\infty}$ is expanded.

$$G_1-G_{1\infty}=\sum_{i=0}^{N}\sum_{j=0}^{N}\sum_{k=0}^{N}C_{ijk}T_i(f_1(X))T_j(f_2(T))T_{2k}(\frac{V}{2}) \tag{A.59}$$

where $f_1(X)=2(X-(N_X-1))-1, f_2(T)=2(T-(N_T-1))-1$.

Furthermore, by substituting $T_n(X)$ into the term G_1-$G_{1\infty}$, the general solutions can simplify the system of equations for calculating the derivative of X, V, and T. The aforementioned calculation process will be used in the hydrodynamic analysis in the air chamber of the buoy.

References:

[1] F. Akhtar, M.H. Rehmani, Energy replenishment using renewable and traditional energy resources for sustainable wireless sensor networks: A review. Renewable and Sustainable Energy Reviews. 45 ((2015) 769-784. 10.1016/j.rser.2015.02.021

[2] M. Bhaskaran, S. Sriram, K.K. Iniewski, Energy harvesting with functional materials and microsystems (2014).

[3] S.K. Chou, W.M. Yang, K.J. Chua, J. Li, K.L. Zhang, Development of micro power generators – a review. Appl. Energ. 88 (1) (2011) 1-16. 10.1016/j.apenergy.2010.07.010

[4] H. Liu, H. Fu, L. Sun, C. Lee, E.M. Yeatman, Hybrid energy harvesting technology: From

materials, structural design, system integration to applications. Renewable and Sustainable Energy Reviews. 137 ((2021) 110473. 10.1016/j.rser.2020.110473

[5] D.L. O Sullivan, A.W. Lewis, Generator selection and comparative performance in offshore oscillating water column ocean wave energy converters. IEEE T. Energy Conver. 26 (2) (2011) 603-614. 10.1109/TEC.2010.2093527

[6] A.F.O. Falcão, J.C.C. Henriques, Oscillating-water-column wave energy converters and air turbines: A review. Renew. Energ. 85 ((2016) 1391-1424. 10.1016/j.renene.2015.07.086

[7] A. Elhanafi, G. Macfarlane, A. Fleming, Z. Leong, Scaling and air compressibility effects on a three-dimensional offshore stationary OWC wave energy converter. Appl. Energ. 189 ((2017) 1-20. 10.1016/j.apenergy.2016.11.095

[8] M. Shalby, D.G. Dorrell, P. Walker, Multi-chamber oscillating water column wave energy converters and air turbines: A review. Int. J. Energ. Res. 43 (2) (2019) 681-696. 10.1002/er.4222

[9] S. Jeong, S. Kim, H. Lee, J. Park, Simulation of hydropower turbine performance in duct for system utilizing tidal jet generator. J. Mech. Sci. Technol. 31 (12) (2017) 5871-5877. 10.1007/s12206-017-1130-0

[10] N. Ansarifard, A. Fleming, A. Henderson, S.S. Kianejad, S. Chai, J. Orphin, Comparison of inflow and outflow radial air turbines in vented and bidirectional OWC wave energy converters. Energy. 182 ((2019) 159-176. 10.1016/j.energy.2019.06.041

[11] T. Zhao, M. Xu, X. Xiao, Y. Ma, Z. Li, Z.L. Wang, Recent progress in blue energy harvesting for powering distributed sensors in ocean. Nano Energy. 88 ((2021) 106199. 1 10.1016/j.nanoen.2021.106199

[12] P.D. Mitcheson, P. Miao, B.H. Stark, E.M. Yeatman, A.S. Holmes, T.C. Green, MEMS electrostatic micropower generator for low frequency operation. Sensors and Actuators A: Physical. 115 (2-3) (2004) 523-529. 10.1016/j.sna.2004.04.026

[13] X. Guo, Y. Zhang, K. Fan, C. Lee, F. Wang, A comprehensive study of non-linear air damping and “pull-in” effects on the electrostatic energy harvesters. Energ. Convers. Manage. 203 ((2020) 112264. 10.1016/j.enconman.2019.112264

[14] K. Tao, J. Wu, L. Tang, L. Hu, S.W. Lye, J. Miao, Enhanced electrostatic vibrational energy harvesting using integrated opposite-charged electrets. J. Micromech. Microeng. 27 (4) (2017) 44002. 1 10.1088/1361-6439/aa5e73

[15] B. Maamer, A. Boughamoura, A.M.R. Fath El-Bab, L.A. Francis, F. Tounsi, A review on design improvements and techniques for mechanical energy harvesting using piezoelectric and electromagnetic schemes. Energ. Convers. Manage. 199 ((2019) 111973. 10.1016/j.enconman.2019.111973

[16] G. Moretti, P.G. Rosati, L. Daniele, D. Forehand, D. Ingram, R. Vertechy, M. Fontana, Modelling and testing of a wave energy converter based on dielectric elastomer generators. Proc Math Phys Eng Sci. 475 (2222) (2019) 20180566. 10.1098/rspa.2018.0566

[17] C.L. Zhang, Z.H. Lai, X.X. Rao, J.W. Zhang, D. Yurchenko, Energy harvesting from a novel contact-type dielectric elastomer generator. Energ. Convers. Manage. 205 ((2020) 112351. 10.1016/j.enconman.2019.112351

[18] K. Xia, J. Fu, Z. Xu, Multiple‐frequency high‐output triboelectric nanogenerator based on a water balloon for all‐weather water wave energy harvesting. Adv. Energy Mater. 10 (28) (2020) 2000426. 10.1002/aenm.202000426

[19] A. Erturk, D.J. Inman, Piezoelectric energy harvesting, in:A. Erturk, D.J. Inman (eds.), John

Wiley & Sons, Ltd, Chichester, UK, 2011, pp. 301-324.
[20] M. Safaei, H.A. Sodano, S.R. Anton, A review of energy harvesting using piezoelectric materials: State-of-the-art a decade later (2008-2018). Smart Mater. Struct. 28 (11) (2019) 113001. 1 10.1088/1361-665X/ab36e4
[21] N. Sezer, M. Koç, A comprehensive review on the state-of-the-art of piezoelectric energy harvesting. Nano Energy. 80 ((2021) 105567. 10.1016/j.nanoen.2020.105567
[22] H. Mutsuda, Y. Tanaka, R. Patel, Y. Doi, Y. Moriyama, Y. Umino, A painting type of flexible piezoelectric device for ocean energy harvesting. Appl. Ocean Res. 68 ((2017) 182-193. 10.1016/j.apor.2017.08.008
[23] G. Moretti, G. Malara, A. Scialò, L. Daniele, A. Romolo, R. Vertechy, M. Fontana, F. Arena, Modelling and field testing of a breakwater-integrated U-OWC wave energy converter with dielectric elastomer generator. Renew. Energ. 146 ((2020) 628-642. 10.1016/j.renene.2019.06.077
[24] J. Chen, S.K. Oh, N. Nabulsi, H. Johnson, W. Wang, J. Ryou, Biocompatible and sustainable power supply for self-powered wearable and implantable electronics using III-nitride thin-film-based flexible piezoelectric generator. Nano Energy. 57 ((2019) 670-679. 10.1016/j.nanoen.2018.12.080
[25] H.S. Kim, J. Kim, J. Kim, A review of piezoelectric energy harvesting based on vibration. Int. J. Precis. Eng. Man. 12 (6) (2011) 1129-1141. 10.1007/s12541-011-0151-3
[26] N. Wu, Q. Wang, X. Xie, Ocean wave energy harvesting with a piezoelectric coupled buoy structure. Appl. Ocean Res. 50 ((2015) 110-118. 10.1016/j.apor.2015.01.004
[27] H.L. Dai, A. Abdelkefi, L. Wang, Piezoelectric energy harvesting from concurrent vortex-induced vibrations and base excitations. Nonlinear Dynam. 77 (3) (2014) 967-981. 10.1007/s11071-014-1355-8
[28] A. Garg, S.K. Dwivedy, Piezoelectric energy harvester under parametric excitation: A theoretical and experimental investigation. J. Intel. Mat. Syst. Str. 31 (4) (2020) 612-631. 10.1177/1045389X19891523
[29] X. Xie, Z. Wang, D. Liu, G. Du, J. Zhang, An experimental study on a novel cylinder harvester made of L-shaped piezoelectric coupled beams with a high efficiency. Energy. 212 ((2020) 118752. 10.1016/j.energy.2020.118752
[30] M. WH, Origin and generation of waves, 1951.
[31] H. Fu, X. Mei, D. Yurchenko, S. Zhou, Rotational energy harvesting for self-powered sensing. Joule (2021).
[32] K. Fan, H. Qu, Y. Wu, T. Wen, F. Wang, Design and development of a rotational energy harvester for ultralow frequency vibrations and irregular human motions. Renew. Energ. 156 ((2020) 1028-1039. 10.1016/j.renene.2020.04.117
[33] S. Chen, R. Yang, G. Wu, C. Wu, A piezoelectric Wave-Energy converter equipped with a Geared-Linkage-Based frequency Up-Conversion mechanism. Sensors-Basel. 21 (1) (2021) 204. 10.3390/s21010204
[34] Z. Lin, Y. Zhang, Dynamics of a mechanical frequency up-converted device for wave energy harvesting. J. Sound Vib. 367 ((2016) 170-184. 10.1016/j.jsv.2015.12.048
[35] N.V. Viet, X.D. Xie, K.M. Liew, N. Banthia, Q. Wang, Energy harvesting from ocean waves by a floating energy harvester. Energy. 112 ((2016) 1219-1226. 10.1016/j.energy.2016.07.019
[36] F. Qian, S. Zhou, L. Zuo, Improving the off-resonance energy harvesting performance using dynamic magnetic preloading. Acta Mech. Sinica-PRC. 36 (3) (2020) 624-634.

10.1007/s10409-020-00929-4
[37] Y. Wu, S. Li, K. Fan, H. Ji, J. Qiu, Investigation of an ultra-low frequency piezoelectric energy harvester with high frequency up-conversion factor caused by internal resonance mechanism. Mech. Syst. Signal Pr. 162 ((2022) 108038. 10.1016/j.ymssp.2021.108038
[38] S. Chen, L. Ma, T. Chen, H. Liu, L. Sun, J. Wang, Modeling and verification of a piezoelectric frequency-up-conversion energy harvesting system. Microsystem Technologies. 23 (7) (2017) 2459-2466. 10.1007/s00542-016-3077-y
[39] H. Liang, G. Hao, O.Z. Olszewski, A review on vibration-based piezoelectric energy harvesting from theaspect of compliant mechanisms. Sensors and Actuators (2021).
[40] J. Falnes, Ocean Waves and Oscillating Systems Linear Interactions Including Wave-Energy Extraction by Johannes Falnes (z-lib.org), 2002.
[41] A. Abdelkefi, Aeroelastic energy harvesting: A review. Int. J. Eng. Sci. 100 ((2016) 112-135. 10.1016/j.ijengsci.2015.10.006
[42] X. Du, Y. Zhao, G. Liu, M. Zhang, Y. Wang, H. Yu, Enhancement of the piezoelectric cantilever beam performance via Vortex-Induced vibration to harvest ocean wave energy. Shock Vib. 2020 ((2020) 1-11. 10.1155/2020/8858529
[43] F. Fei, J.D. Mai, W.J. Li, A wind-flutter energy converter for powering wireless sensors. Sensors and Actuators A: Physical. 173 (1) (2012) 163-171. 10.1016/j.sna.2011.06.015
[44] A. Abdelkefi, A.H. Nayfeh, M.R. Hajj, Design of piezoaeroelastic energy harvesters. Nonlinear Dynam. 68 (4) (2012) 519-530. 10.1007/s11071-011-0233-x
[45] F. Ewere, G. Wang, Performance of galloping piezoelectric energy harvesters. J. Intel. Mat. Syst. Str. 25 (14) (2014) 1693-1704. 10.1177/1045389X13505251
[46] G. Hu, J. Wang, L. Tang, A comb-like beam based piezoelectric system for galloping energy harvesting. Mech. Syst. Signal Pr. 150 ((2021) 107301. 10.1016/j.ymssp.2020.107301
[47] S. Jo, W. Sun, C. Son, J. Seok, Galloping-based energy harvester considering enclosure effect. AIP Adv. 8 (9) (2018) 95309. 10.1063/1.5043586
[48] J. Jia, X. Shan, D. Upadrashta, T. Xie, Y. Yang, R. Song, Modeling and analysis of upright piezoelectric energy harvester under aerodynamic vortex-induced vibration. Micromachines-Basel. 9 (12) (2018) 667. 10.3390/mi9120667
[49] D. Zhao, J. Zhou, T. Tan, Z. Yan, W. Sun, J. Yin, W. Zhang, Hydrokinetic piezoelectric energy harvesting by wake induced vibration. Energy. 220 ((2021) 119722. 10.1016/j.energy.2020.119722
[50] F. Pan, Z. Xu, L. Jin, P. Pan, X. Gao, Designed simulation and experiment of a piezoelectric energy harvesting system based on Vortex-Induced vibration. IEEE T. Ind. Appl. 53 (4) (2017) 3890-3897. 10.1109/TIA.2017.2687401
[51] X. Shan, R. Song, B. Liu, T. Xie, Novel energy harvesting: A macro fiber composite piezoelectric energy harvester in the water vortex. Ceram. Int. 41 ((2015) S763-S767. 10.1016/j.ceramint.2015.03.219
[52] J. Oh, J. Jang, OWC design to increase wave energy absorption efficiency in wave conversion systems. J. Mech. Sci. Technol. 29 (7) (2015) 2987-2993. 10.1007/s12206-015-0629-5
[53] W. Song, Thermal transfer analysis of a freezing soil medium with an embedded pipeline. J. Cold Reg. Eng. 20 (1) (2006) 20-36. 1 10.1061/(ASCE)0887-381X(2006)20:1(20)
[54] C.C. Mei, M. Stiassnie, D.K.P. Yue, Theory and applications of ocean surface waves., World Scientific Publishing Company., 2005.

[55] T. Miloh, P.A. Tyvand, G. Zilman, Green functions for initial free-surface flows due to 3D impulsive bottom deflections. J. Eng. Math. 43 (1) (2002) 57-74. 1 10.1023/A:1016505628660
[56] A.B. Finkelstein, The initial value problem for transient water waves. Communication on pure and applied mathematics. x (vol) (1957) 511-522.
[57] X. Du, M. Zhang, H. Kang, H. Chang, H. Yu, Theoretical study on a novel piezoelectric ocean wave energy harvester driven by oscillating water column. Energy sources. Part A, Recovery, utilization, and environmental effects (2021) 1-21. 1 10.1080/15567036.2020.1862367
[58] A.J.N.A. Sarmento, A.F.D.O. Falcão, Wave generation by an oscillating surface-pressure and its application in wave-energy extraction. J. Fluid Mech. 150 ((1985) 467-485. 1 10.1017/S0022112085000234
[59] R. A, On the development of turbulent wakes from vortex streets (1954) 8, 9, 24.
[60] L.A. Weinstein, M.R. Cacan, P.M. So, P.K. Wright, Vortex shedding induced energy harvesting from piezoelectric materials in heating, ventilation and air conditioning flows. SMART MA TERIALS AND STRUCTURES (2012).
[61] Y. Hu, B. Yang, X. Chen, X. Wang, J. Liu, Modeling and experimental study of a piezoelectric energy harvester from vortex shedding-induced vibration. Energ. Convers. Manage. 162 ((2018) 145-158. 10.1016/j.enconman.2018.02.026
[62] R. A, On the development of turbulent wakes from vortex streetsp8) (1954).
[63] J.P. Ayers, D.W. Greve, I.J. Oppenheim, Energy scavenging for sensor applications using structural strains. 5057 (2003) 364-375. 10.1117/12.482377.
[64] P.D. Mitcheson, P. Miao, B.H. Stark, E.M. Yeatman, A.S. Holmes, T.C. Green, MEMS electrostatic micropower generator for low frequency operation. Sensors and Actuators A: Physical. 115 (2-3) (2004) 523-529. 10.1016/j.sna.2004.04.026
[65] A. Iturrioz, R. Guanche, J.L. Lara, C. Vidal, I.J. Losada, Validation of OpenFOAM® for Oscillating Water Column three-dimensional modeling. Ocean Eng. 107 ((2015) 222-236. 10.1016/j.oceaneng.2015.07.051
[66] J.M. Paixão Conde, L.M.C. Gato, Numerical study of the air-flow in an oscillating water column wave energy converter. Renew. Energ. 33 (12) (2008) 2637-2644. 10.1016/j.renene.2008.02.028
[67] A. Kamath, H. Bihs, Ø.A. Arntsen, Numerical investigations of the hydrodynamics of an oscillating water column device. Ocean Eng. 102 ((2015) 40-50. 10.1016/j.oceaneng.2015.04.043
[68] C. Xu, Z. Huang, Three-dimensional CFD simulation of a circular OWC with a nonlinear power-takeoff: Model validation and a discussion on resonant sloshing inside the pneumatic chamber. Ocean Eng. 176 ((2019) 184-198. 10.1016/j.oceaneng.2019.02.010
[69] A. Elhanafi, G. Macfarlane, A. Fleming, Z. Leong, Experimental and numerical measurements of wave forces on a 3D offshore stationary OWC wave energy converter. Ocean Eng. 144 ((2017) 98-117. 10.1016/j.oceaneng.2017.08.040
[70] T. Vyzikas, S. Deshoulières, O. Giroux, M. Barton, D. Greaves, Numerical study of fixed Oscillating Water Column with RANS-type two-phase CFD model. Renew. Energ. 102 ((2017) 294-305. 10.1016/j.renene.2016.10.044
[71] J.F. Derakhshandeh, Analysis of wake induced vibration of a coupled circular cylinder-piezoelectric using two-way fluid structural interaction. Appl. Ocean Res. 121 ((2022) 103116. 10.1016/j.apor.2022.103116
[72] W. Sun, J. Seok, Novel galloping-based piezoelectric energy harvester adaptable to external wind velocity. Mech. Syst. Signal Pr. 152 ((2021) 107477. 1 10.1016/j.ymssp.2020.107477

[73] T. Tan, L. Zuo, Z. Yan, Environment coupled piezoelectric galloping wind energy harvesting. Sensors and Actuators A: Physical. 323 ((2021) 112641. 10.1016/j.sna.2021.112641

[74] T. Zhao, M. Xu, X. Xiao, Y. Ma, Z. Li, Z.L. Wang, Recent progress in blue energy harvesting for powering distributed sensors in ocean. Nano Energy. 88 ((2021) 106199. 10.1016/j.nanoen.2021.106199

[75] A. Haroun, X. Le, S. Gao, B. Dong, T. He, Z. Zhang, F. Wen, S. Xu, C. Lee, Progress in micro/nano sensors and nanoenergy for future AIoT-based smart home applications. Nano express. 2 (2) (2021) 22005. 1 10.1088/2632-959X/abf3d4

[76] H. Yu, C. Hou, X. Shan, X. Zhang, H. Song, X. Zhang, T. Xie, A novel seesaw-like piezoelectric energy harvester for low frequency vibration. Energy. 261 ((2022) 125241. 10.1016/j.energy.2022.125241

[77] G. Shi, D. Tong, Y. Xia, S. Jia, J. Chang, Q. Li, X. Wang, H. Xia, Y. Ye, A piezoelectric vibration energy harvester for multi-directional and ultra-low frequency waves with magnetic coupling driven by rotating balls. Appl. Energ. 310 ((2022) 118511. 10.1016/j.apenergy.2021.118511

[78] L. Zhao, H. Zou, Z. Wu, Q. Gao, G. Yan, F. Liu, K. Wei, W. Zhang, Dynamically synergistic regulation mechanism for rotation energy harvesting. Mech. Syst. Signal Pr. 169 ((2022) 108637. 10.1016/j.ymssp.2021.108637

[79] Y. Wu, S. Li, K. Fan, H. Ji, J. Qiu, Investigation of an ultra-low frequency piezoelectric energy harvester with high frequency up-conversion factor caused by internal resonance mechanism. Mech. Syst. Signal Pr. 162 ((2022) 108038. 10.1016/j.ymssp.2021.108038

[80] Y. Wang, X. Liu, Y. Wang, H. Wang, H. Wang, S.L. Zhang, T. Zhao, M. Xu, Z.L. Wang, Flexible Seaweed-Like triboelectric nanogenerator as a wave energy harvester powering marine internet of things. ACS Nano. 15 (10) (2021) 15700-15709. 10.1021/acsnano.1c05127

[81] S. Chen, R. Yang, G. Wu, C. Wu, A piezoelectric Wave-Energy converter equipped with a Geared-Linkage-Based frequency Up-Conversion mechanism. Sensors-Basel. 21 (1) (2021) 204. 10.3390/s21010204

[82] M.A. Halim, M.H. Kabir, H. Cho, J.Y. Park, A frequency Up-Converted hybrid energy harvester using transverse Impact-Driven piezoelectric bimorph for Human-Limb motion. Micromachines-Basel. 10 (10) (2019) 701. 10.3390/mi10100701

[83] M. Li, J. Zhou, X. Jing, Improving low-frequency piezoelectric energy harvesting performance with novel X-structured harvesters. Nonlinear Dynam. 94 (2) (2018) 1409-1428. 10.1007/s11071-018-4432-6

[84] W.S. Hwang, J.H. Ahn, S.Y. Jeong, H.J. Jung, S.K. Hong, J.Y. Choi, J.Y. Cho, J.H. Kim, T.H. Sung, Design of piezoelectric ocean-wave energy harvester using sway movement. Sensors and Actuators A: Physical. 260 ((2017) 191-197. 10.1016/j.sna.2017.04.026

[85] J.V. Wehausen, E.V. Laitone, Surface waves (1960).

[86] N.J. N, The approximation of free-surface Green functions (1990).

[87] T. Miloh, P.A. Tyvand, G. Zilman, Green functions for initial free-surface flows due to 3D impulsive bottom deflections. J. Eng. Math. 43 (1) (2002) 57-74. 1 10.1023/A:1016505628660

[88] Abramowitz, Milton, Handbook of mathematical functions : With formulas, graphs and mathematical tables | Clc. Am. J. Phys. 56 (10) (1988) 958.

[89] L. Fox, I.B. Parker, Chebyshev polynomials in numerical analysis (1968).

Xiaozhen Du received his Ph.D. from Dalian University of Technology (Dalian, China) in 2008. He is now the Professor of the College of Mechanical and Electronic Engineering at Shandong University of Science and Technology (Qingdao, China). His research interests include vibration energy, ocean wave energy, and wind energy harvesting with piezoelectric, electromagnetic, and triboelectric effects for novel integration sensor devices.

Yu Wang received his master's degree in mechanical engineering from Shandong University of Science and Technology in 2022. His main research interests are the development and utilization of wave energy.

Haixiang Chen is currently pursuing a master's degree in mechanical engineering at Shandong University of Science and Technology (Qingdao, China). His research interests focus on ocean wave energy harvesting and self-powered sensing devices based on piezoelectric/electromagnetic generators.

Chicheng Li is currently pursuing his master's degree at Shandong University of Science and Technology (Qingdao, China). His main research interests are oscillating water columns ocean wave energy harvesting, air compression energy storage, and piezoelectric energy harvester performance optimization.

Yi Han is currently pursuing his master's degree at Shandong University of Science and Technology (Qingdao, China). His main research interests are hybrid energy harvesting and self-powered sensing devices based on triboelectric nanogenerators and piezoelectric energy harvesters.

Dr. Yurchenko is an expert in the area of nonlinear stochastic dynamics, vibrations mitigation and energy harvesting with focus on mathematical and experimental modeling of complex dynamic systems. He obtained a Ph.D degree in Mechanical Engineering from Worcester Polytechnic Institute, USA. He worked as Professor at Saint-Petersburgh Technical University and joined ISVR in 2022. He is a recipient of the prestigious Russian Young Scientists award, several research grants, including EPSRC and the Royal Society awards. He is a member of the EUROMECH, Editorial board member of Mechanical Systems and Signal Processing, Int. J. of Dynamics and Control, Vibrations, Energies.

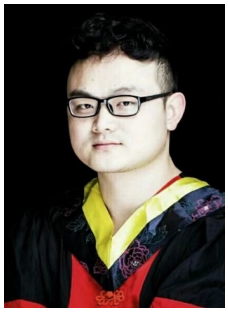

Dr. Junlei Wang received his B.E degree and Ph.D in the School of Power Engineering at Chongqing University in 2009 and 2014, respectively. He was also a visiting scholar of Mechanical Engineering at the University of Auckland, New Zealand from 2019 to 2020. His main research interests include flow-induced vibrations suppression, flow energy harvesting, triboelectric, piezoelectric and hybrid energy harvesting technology. Dr. Wang is the recipient of three times National Natural Science Foundation of China (NSFC), Grant No: 51606071, 51977196 and 52277227. Hi is leading Editors of Journal of Physics D: Applied Physics, and ASCE Journal of Environmental Engineering.

Dr. Hong Yu is an Associate Professor in the College of Science at China University of Petroleum (East China). She received her Ph.D. at State Key Laboratory of Materials Modification by Electron, Ion and Laser Beams, Dalian University of Technology in 2006. Her current research is mainly focused on the areas of piezoelectric and triboelectric nanogenerator performance optimization and low-temperature plasma physics and applications.